

Anomalous transport properties and electronic
states of narrow-gap semiconductor FeSb_2
(ナローギャップ半導体 FeSb_2 における異常
輸送現象と電子状態)

高橋 英史

Contents

1	Introduction	1
1.1	Background	1
1.2	Seebeck effect and thermoelectric efficiency	3
1.2.1	Boltzmann equation	3
1.2.2	Seebeck coefficient	5
1.2.3	Thermoelectric efficiency	8
1.3	Narrow-gap semiconductor FeSb ₂	10
1.3.1	Huge Seebeck coefficient of FeSb ₂	10
1.3.2	Crystal structure of FeSb ₂	13
1.3.3	Magnetic property	16
1.3.4	Resistivity and Hall coefficient	17
1.3.5	Band structure calculation	18
2	Ppm-level impurity effect of transport properties on single crystal	22
2.1	Introduction	22
2.2	Experiment	22
2.2.1	Sample preparation method	22
2.2.2	Experimental methods of the magnetic susceptibility and transport properties	23
2.3	Result and Discussion	25
2.3.1	Magnetic susceptibility	25
2.3.2	Electrical resistivity	25
2.3.3	Hall coefficient	26
2.3.4	Carrier concentration and mobility	28
2.3.5	Seebeck coefficient	30
2.3.6	Power factor	31
2.4	Summary	33
3	Magnetotransport properties	35
3.1	Introduction	35
3.2	Experiment	35

3.3	Result and discussion	36
3.3.1	Temperature dependence of the magnetoresistance	36
3.3.2	Magnetic field dependence of the magnetoresistance and the Hall resistivity	37
3.3.3	Magnetic field dependence of the magnetoconductivity tensor	37
3.3.4	Temperature dependence of the carrier concentration and mobility	39
3.3.5	Magnetotransport properties below 4 K	41
3.4	Summary	43
4	Pressure effect of transport properties to analyze the gap formation mechanism	44
4.1	Introduction	44
4.2	Experiment	45
4.3	Results and Discussion	45
4.3.1	Pressure effect of the electrical resistivity	45
4.3.2	Pressure dependence of the magnetotransport properties	49
4.3.3	Analysis of the pressure dependence of the carrier concentration and the mobility	49
4.3.4	Origin of the gap enhancement of Δ_1	49
4.3.5	Origin of the gap enhancement of Δ_2 : Association with the Kondo mechanism.	54
4.3.6	Origin of the huge Seebeck coefficient	54
4.4	Summary	56
5	Conclusion	58

Chapter 1

Introduction

1.1 Background

Electrons in a solid carry electrical charge and heat, and thus electric and heat currents are driven by an electric field and temperature gradient. The electric and heat currents have a cross-correlation, which is known as the thermoelectric effects. One example is the Seebeck effect. This is a phenomenon that the temperature gradient in a metal or semiconductor generates the electric field, and the proportionality coefficient is called " Seebeck coefficient. " From the phenomenological analysis of the nonequilibrium phenomenon, the Seebeck coefficient is closely related to the entropy of the conduction electrons in the solid. Thus, the Seebeck coefficient is an interesting parameter to investigate physical properties of materials because this can provide important information, such as the entropy due to the charge and spin degrees of freedom in conduction electrons.

Recently, the thermoelectric effects have attracted much attention as the application for the environmental conservation. In 1987, the United Nations proposed a concept of "Sustainable Development", which is a central guideline to solve the environmental problem, and defined this word as "Sustainable development is development that meets the needs of the present without compromising the ability of future generations to meet their own needs." One example about these needs is "energy resources." Currently, oil and coal are mainly used as primary energy resources, but these energy resources might be exhausted and give a load in the environment. Using the thermoelectrics, energy conversion technology using the thermoelectric phenomena, we can directly convert heat energy into electric energy with the Seebeck and Peliter effects. Thus, we can reduce the consumption of primary energy resources, since unused heat can produce the electricity. Moreover, this technology is available as a refrigerator without gases and mechanical moving parts, contributing to the saving of the environment and resources.

The thermoelectricity was discovered by Seebeck in the nineteenth century.[1] From 1950s to 1960s, good thermoelectric materials have been synthesized in doped semiconductors such as bismuth telluride and lead telluride,[2] and models to explain these good thermoelectric properties have been established.[3, 4, 5, 6, 7] However, the quantity of material resources is poor as commercial uses, and in spite of the discovery of these materials, the study of thermoelectric materials was rather slowly developed.

In 1990s, a significant increase of investigation for thermoelectric materials occurred. As one factor, new material design guidelines such as “Low dimensional structure” and “Phonon glass and electron crystal” are proposed.[8, 9] Based on these concepts, nanostructure materials (superlattice film and quantum wire, etc.) and unique structure materials (skutterudite and clathrate compounds, etc.) are investigated.[10, 11] As another factor, there are numerous investigations of the strong-electron correlated systems for the last two decades, in which *d*- or *f*-orbital electrons act an important role in transport properties. In *d*-electron systems, unique physical properties such as the high-temperature superconductivity in Cu oxides, have been observed.[12] Among them, NaCo_2O_4 (Na_xCoO_2) shows a high performance as a thermoelectric material,[13] which is thought to be realized due to the spin and orbital degrees of freedom of *3d* orbitals. Since this discovery, the extensive studies are conducted in the transition metal oxides. Heavy fermions, which are mainly realized in *f*-orbital systems, are also expected to be thermoelectric materials at low temperatures.[14, 15] These materials show a low resistivity and a large Seebeck coefficient at the same time, which are the necessary conditions for thermoelectric materials, because the effective mass of electrons becomes heavy due to the coupling between conduction bands and *f*-orbital bands near the Fermi level. As described above, many theoretical and experimental studies have progressed for the search of thermoelectric materials, indicating that the investigation for thermoelectric materials is spread over not only material engineering but also condensed matter physics.

Recently, a huge Seebeck coefficient of -45 mV/K at 10 K was reported in a single crystal of FeSb_2 . [16] This huge value cannot be explained by conventional theories, which reminds us of a novel physics. In addition, this material is remarked because of a potential application as the Peltier device in the low temperature due to this huge value. However, a polycrystalline sample of FeSb_2 shows a much smaller value of the Seebeck coefficient (~ -500 $\mu\text{V/K}$), and a large sample dependence of this value is observed. [17, 18] In spite of extensive studies, the origin of this huge Seebeck coefficient and the large sample dependence have not been revealed. In order to address these issues, we first investigate the ppm-level impurity effect on single crystals to elucidate a reason of the large sample dependence of the physical properties. Through the systematic study of impurity effects, we unravel the large sample dependence, and observe the large

Seebeck coefficient in a purest sample. Thus, we next study the magnetotransport properties on the purest sample at low temperature, which can elucidate the electronic states in this compound: There is a small energy gap of 30 meV. Since the large Seebeck coefficient is observed below 40 K, some groups suggest a possibility that the small energy gap is formed by an unusual mechanism such as a strong electron correlation anticipated in the Kondo insulators. For this suggestion, we conduct transport measurements under pressure and evaluate the pressure dependence of the energy gap size because the gap size of Kondo insulators is sensitive to a compression of the lattice size. We propose a model of the gap formation mechanism and an origin of the huge Seebeck coefficient from the above studies.

This thesis is organized as follows: In Section 1.2, and 1.3, we introduce a brief theory of the Seebeck effect and physical properties of FeSb₂, respectively. Then, we show above three experimental results in Chapter 2 (Ppm-level impurity effect of transport properties on single crystals), Chapter 3 (Magnetotransport properties), and Chapter 4 (Pressure effect of transport properties to analyze the gap formation mechanism). Finally, we summarize all the results in Chapter 5.

1.2 Seebeck effect and thermoelectric efficiency

1.2.1 Boltzmann equation

Here, we briefly introduce a theory of the Seebeck effect and the thermoelectrics. In the temperature gradient, metals and semiconductors generate an electric voltage, which is called the Seebeck effect. This effect is intrinsically a nonequilibrium phenomenon, and arises from a coupling between the thermal and electric phenomena. To analyze the nonequilibrium phenomena, we use the Boltzmann equation.[19] The Boltzmann equation is a formula to calculate a distribution function $f(\mathbf{k}, \mathbf{r}; t)$ in external fields, such as the electric field and the temperature gradient. In the weak field limit, $f(\mathbf{k}, \mathbf{r}; t)$ can be written by $f = f_0 + f_1$, where f_0 and f_1 are the distribution function at the equilibrium state and the deviation from this, respectively. The time evolution of $f(\mathbf{k}, \mathbf{r}; t)$ can be described as

$$\frac{\partial f}{\partial t} = \left(\frac{\partial f}{\partial t}\right)_{drift} + \left(\frac{\partial f}{\partial t}\right)_{diff} + \left(\frac{\partial f}{\partial t}\right)_{scatt}. \quad (1.1)$$

Here, $\left(\frac{\partial f}{\partial t}\right)_{drift}$ is due to drift of carriers in external fields. $\left(\frac{\partial f}{\partial t}\right)_{diff}$ is a diffusion term which means a change of a carrier position with velocity \mathbf{v} . $\left(\frac{\partial f}{\partial t}\right)_{scatt}$ comes from scattering with scatterers and another electrons. The drift and diffusion terms are finally described as

$$\left(\frac{\partial f}{\partial t}\right)_{drift} + \left(\frac{\partial f}{\partial t}\right)_{diff} = -\frac{\mathbf{F}}{\hbar} \left(\frac{\partial f}{\partial \mathbf{k}}\right) - \mathbf{v} \left(\frac{\partial f}{\partial \mathbf{r}}\right). \quad (1.2)$$

The scattering term is difficult to solve precisely, and then we usually use the relaxation time approximation as $(\frac{\partial f}{\partial t})_{scatt} = -\frac{1}{\tau}(f - f_0) = -\frac{1}{\tau}f_1$, where τ is the scattering time. Considering an electron system, we can apply the Fermi-Dirac distribution function for $f_0 = [\exp(\epsilon_{\mathbf{k}} - \mu)/k_B T + 1]^{-1}$, where $\epsilon_{\mathbf{k}}$ and μ are eigenenergy with momentum \mathbf{k} and chemical potential, respectively. We further assume that the external field is the electric field and \mathbf{r} dependence of f only through the space variation of temperature $T(\mathbf{r})$. In the above assumption, we obtain the deviation function in the steady state ($\frac{\partial f}{\partial t} = 0$) as

$$f_1 = (-\frac{\partial f_0}{\partial \epsilon})\mathbf{v}_{\mathbf{k}}\tau[e\mathbf{E} + \frac{\epsilon - \mu}{T}(-\nabla T)]. \quad (1.3)$$

Here, we use the following expression of the group velocity given by

$$\mathbf{v}_{\mathbf{k}} = \frac{1}{\hbar} \frac{\partial \epsilon_{\mathbf{k}}}{\partial \mathbf{k}}. \quad (1.4)$$

Using Eq. (1.3), we can calculate the electrical density as

$$\mathbf{j} = \frac{1}{4\pi^3} \int e\mathbf{v}_{\mathbf{k}} f_1 d^3 k. \quad (1.5)$$

The prefactor of $1/4\pi^3 = 2/(2\pi)^3$ represents the density of states for the momentum space times the spin degrees of freedom. The thermal current is also calculated in the same way. We can define the heat per electron as $\epsilon_{\mathbf{k}} - \mu$, and the thermal current as

$$\mathbf{q} = \frac{1}{4\pi^3} \int (\epsilon_{\mathbf{k}} - \mu)\mathbf{v}_{\mathbf{k}} f_1 d^3 k. \quad (1.6)$$

Substituting Eq. (1.3) in Eqs. (1.5) and (1.6), we obtain

$$\mathbf{j} = e^2 \hat{K}_0 \mathbf{E} + \frac{e}{T} \hat{K}_1 (-\nabla T) \quad (1.7)$$

$$\mathbf{q} = e \hat{K}_1 \mathbf{E} + \frac{1}{T} \hat{K}_2 (-\nabla T), \quad (1.8)$$

where

$$\hat{K}_n = \frac{1}{4\pi} \int (-\frac{\partial f_0}{\partial \epsilon}) \mathbf{v}_{\mathbf{k}} \mathbf{v}_{\mathbf{k}} \tau (\epsilon_{\mathbf{k}})^n d^3 k. \quad (1.9)$$

In this equation, \hat{K}_n is a second-rank tensor. From the Eqs. (1.7) and (1.8), transport coefficients are given by the following equations, in which all parameters are reduced to scalar quantities for a cubic crystal:

$$\sigma = e^2 K_0, \quad (1.10)$$

$$S = \frac{1}{eT} \frac{K_1}{K_0}, \quad (1.11)$$

$$\kappa' = \frac{K_2}{T}, \quad (1.12)$$

where σ , S and κ' are the electrical conductivity, Seebeck coefficient, and thermal conductivity in the absence of the electric field. We can simplify Eqs. (1.7) and (1.8) with these parameters as

$$\mathbf{j} = \sigma \mathbf{E} + S\sigma(-\nabla T), \quad (1.13)$$

$$\mathbf{q} = S\sigma T \mathbf{E} + \kappa'(-\nabla T). \quad (1.14)$$

1.2.2 Seebeck coefficient

The Seebeck effect is a phenomenon, in which the electric field ($\mathbf{E} = -\nabla V$) is generated by the temperature gradient ($-\nabla T$), determined as

$$\nabla V = S(-\nabla T). \quad (1.15)$$

From the Boltzmann equation, the Seebeck coefficient is given as

$$\begin{aligned} S &= \frac{1}{eT} \frac{K_1}{K_0} \\ &= \frac{1}{eT} \frac{\int (-\frac{\partial f_0}{\partial \epsilon}) v_{\mathbf{k}}^2 \tau(\epsilon_{\mathbf{k}} - \mu) d^3 k}{\int (-\frac{\partial f_0}{\partial \epsilon}) v_{\mathbf{k}}^2 \tau d^3 k}. \end{aligned} \quad (1.16)$$

Here, we change the integral of k to the integral of ϵ , and assume that an isotropic band structure. The Seebeck coefficient can be described by

$$S = \frac{1}{eT} \frac{\int (-\frac{\partial f_0}{\partial \epsilon}) L(\epsilon) (\epsilon - \mu) d\epsilon}{\int (-\frac{\partial f_0}{\partial \epsilon}) L(\epsilon) d\epsilon}, \quad (1.17)$$

where, $L(\epsilon) \simeq D(\epsilon) v_x^2(\epsilon) \tau(\epsilon)$: $D(\epsilon)$ is the density of states and v_x is the carrier velocity along the x direction.

First, we apply Eq. (1.17) to a non-degenerate semiconductor.[15] In the case of the n(p)-type semiconductor, we only integrate Eq. (1.17) above (below) the band edge E_c (E_v). Moreover, when the energy gap $E_c - \mu$ ($\mu - E_v$) is much larger than $k_B T$, f_0 can be approximated as the Maxwell-Boltzmann distribution function. Thus, the Seebeck coefficient of the semiconductor can be described by

$$S(T) \approx \frac{k_B}{e} \left[\frac{(E_c - \mu)}{k_B T} + r \right] \quad (\text{n-type}), \quad (1.18)$$

and

$$S(T) \approx \frac{k_B}{e} \left[\frac{(\mu - E_v)}{k_B T} + r \right] \quad (\text{p-type}), \quad (1.19)$$

where r is the scattering parameter, which comes from the integral of τ . From these equations, we see that the energy gap and r are the material parameters to determine the value of the Seebeck coefficient.

Next, we think about a degenerate (metallic) system. Here, we apply the Sommerfeld expansion of $L(\epsilon) = L(\mu) + L'(\mu)(\epsilon - \mu) + \dots$ in Eq. (1.17). The Seebeck coefficient is expressed by

$$S(T) \simeq -\frac{\pi^2 k_B^2}{3e} \frac{L'(\mu)}{L(\mu)} T, \quad (1.20)$$

where we neglect the terms after 3rd term of the Sommerfeld expansion. This expression indicates that the value of the Seebeck coefficient is proportional to the energy derivative of the density of states.

At low temperature, the carrier conductivity σ (Eq. (1.10)) can be written by $e^2 L(\mu)$. The Seebeck coefficient is expressed with σ by

$$S(T) \simeq -\frac{\pi^2 k_B^2}{3e} T \left[\frac{\partial \ln \sigma(\epsilon)}{\partial \epsilon} \right]_{\epsilon=\mu}. \quad (1.21)$$

This is known as the Mott formula.[20] σ can be described with the carrier concentration $n(\epsilon)$ and the mobility $\mu(\epsilon)$ as $\sigma = n(\epsilon)e\mu(\epsilon)$, and then the Seebeck coefficient is described by

$$S(T) \simeq -\frac{\pi^2 k_B^2}{3e} T \left[\frac{D(\epsilon)}{n} + \frac{\partial \ln \mu(\epsilon)}{\partial \epsilon} \right]_{\epsilon=\mu} \propto \frac{C_{el}}{en} + r, \quad (1.22)$$

where C_{el} is the specific heat of electrons ($\frac{\pi^2}{3} k_B^2 T D(\epsilon)$). This expression shows that the Seebeck coefficient is proportional to the specific heat per carrier. In other words, the Seebeck coefficient is proportional to the entropy per carrier.

In usual metals, the Seebeck coefficient is very small because of the large Fermi energy. When we apply Eq. (1.22) in the 3-dimensional noninteracting Fermi gas, S is expressed as $S = \pm \frac{\pi^2 k_B^2 T}{3e\epsilon_F} (r + \frac{3}{2})$. Thus, S can be written as an universal value of $|k_B/e| = 86 \mu\text{V/K}$ times $k_B T/\epsilon_F$, and a large ϵ_F reduces the Seebeck coefficient. In a typical metal of Cu, a small Seebeck coefficient of $1.7 \mu\text{V/K}$ is observed at room temperature. However, a peculiar large Seebeck coefficient has been reported in the heavy fermion compounds.[15] Figure 1.1(a) shows the temperature dependence of the Seebeck coefficient for Ce-compounds, typical heavy-fermion compounds. A large Seebeck coefficient is observed in CePd₃ in spite of a small resistivity ($\sim 170 \mu\Omega\text{cm}$ at room temperature). The large value of S is due to the large electron specific heat coefficient γ ($C_{el} = \gamma T$). In the heavy fermion compounds, the localized f -electrons and conduction electrons are coupled with the Kondo effect, and the localized electrons move coherently with conduction electrons. Thus, the magnetic entropy of f -electrons is attached

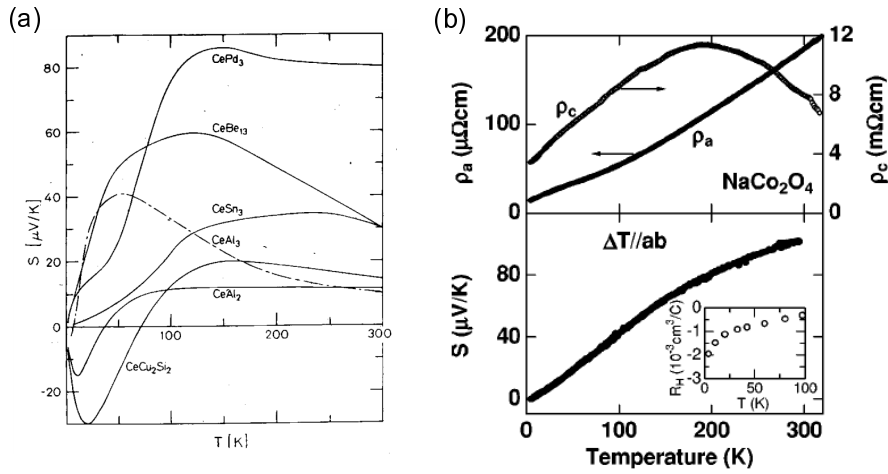


Figure 1.1: (a) The Seebeck coefficient of Ce-compounds.[15] (b) The upper and lower panels show the resistivity and Seebeck coefficient of NaCo_2O_4 , respectively.[13]

to conduction electrons, and the large γ is realized. In other words, the conduction carriers with the large spin entropy of f -electrons result in the enhancement of the Seebeck coefficient.

In the case of the $3d$ transition metal oxides, Na_xCoO_2 shows a large Seebeck coefficient and a metallic resistivity (Fig. 1.1(b)).[13] This origin can be explained by two models. One is an itinerant band model proposed by Kuroki *et al.*[21] They suggest that the large Seebeck coefficient and the small resistivity are due to a unique band structure, which is called as “pudding-mold structure”. In this model, important is a large difference between the carrier velocities above and below the Fermi energy. The other model is based on a localized picture proposed by Koshibae *et al.*[22] They explain the large Seebeck coefficient with spin and orbital degrees of freedom of the Co ions. In the Na_xCoO_2 , the Co^{3+} and Co^{4+} ions are in the low spin state, and the configuration of Co^{3+} is $(t_{2g})^6$ with the entropy of zero, and the configuration of Co^{4+} is $(t_{2g})^5$ with the degeneracy of 6, which comes from the spin part of 2 and the orbital part of 3. In this case, the large entropy is carried due to the large entropy difference between Co^{3+} and Co^{4+} . The Seebeck coefficient is proportional to the entropy per carrier. Thus, the large value is observed because of the large entropy of spin and orbital degrees of freedom for Co ions.

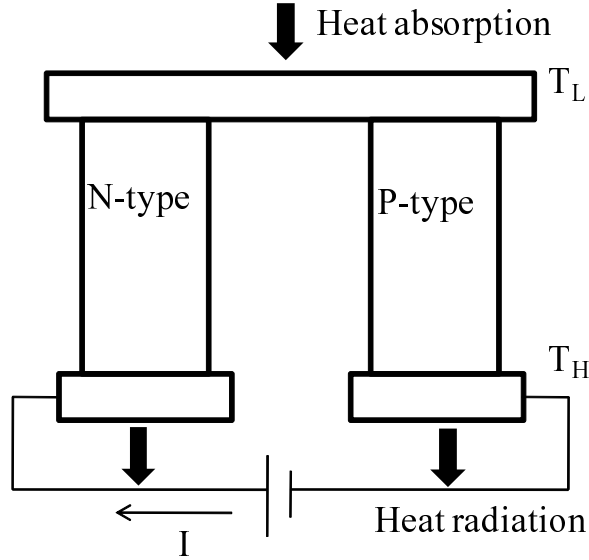


Figure 1.2: A schematic picture of the Peltier cooling device.

1.2.3 Thermoelectric efficiency

For an application, we need to know the efficiency of thermoelectric devices. We use the thermoelectric module as a Peltier cooling, in which thermoelectric materials of n-type and p-type are connected in series as shown in Fig. 1.2. In this system, the upper side of this device absorbs heat and the lower side radiates heat due to the Peltier effect when the electric current is applied. Now, we give a brief introduction of the efficiency of a Peltier refrigerator.[15] We denote the net resistance, net Seebeck coefficient, and net thermal conductivity of the device (Fig. 1.2) as R , S , and K , respectively. For simplicity, we assume that these parameters are independent of temperature. The efficiency of the refrigerator is defined as $\phi = J_{Q_c}/P$: J_{Q_c} is the rate of absorbed heat at the cold side, and P is the input power. J_{Q_c} is described as

$$J_{Q_c} = ST_c I - \frac{1}{2}RI^2 - K\Delta T, \quad (1.23)$$

where the first term comes from the Peltier effect, and the second term is the Joule heat in the sample (we assume that the joule heat equally flows to both the high and low temperature sides.), and the third term is the back flow of the thermal current by the temperature different $\Delta T = (T_H - T_L)$. The input power is given by

$$P = VI = (IR + S\Delta T)I. \quad (1.24)$$

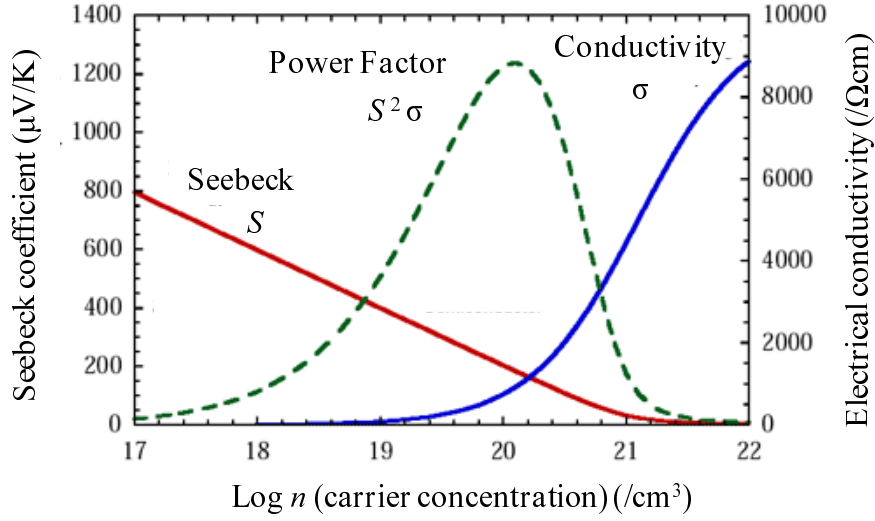


Figure 1.3: The Seebeck coefficient S (red solid curve), conductivity σ (blue solid curve), and power factor $S^2\sigma$ (green dotted curve) as a function of the carrier concentration.

Thus, the efficiency can be expressed by

$$\eta = J_{Q_c}/P = \frac{ST_c I - \frac{1}{2}RI^2 - K\Delta T}{(IR + S\Delta T)I}. \quad (1.25)$$

The maximum value of this efficiency is obtained by taking $d\eta/dI = 0$. After some calculations, the maximum value of this efficiency, which is called as COP (the coefficient of performance), is given by

$$COP = \eta_{max} = \frac{T_c\sqrt{1 + Z\bar{T}} - T_H}{\Delta T(\sqrt{1 + Z\bar{T}} + 1)}, \quad (1.26)$$

where Z is the figure of merit defined by $Z = \frac{S^2}{RK} = \frac{S^2}{\rho\kappa} = \frac{\sigma S^2}{\kappa}$, and $\bar{T} = (T_H + T_L)/2$. According to Eq. (1.26), the dimensionless figure of merit ZT is the most important parameter for thermoelectrics, and the efficiency monotonically increases with increasing ZT value. For commercial uses, it is an aim to be more than 1 in ZT .

Above analysis indicates that the thermoelectric materials are characterized by ZT , and to get a high performance, we need to search materials, which have a large Seebeck coefficient, high electrical conductivity, and low thermal conductivity at the same time. Such requirements are difficult to be satisfied, because

these three parameters are a function of the carrier concentration. In Fig. 1.3, we only depict the carrier concentration dependence of the Seebeck coefficient, electrical conductivity, and power factor ($S^2\sigma$), which is the numerator of the figure of merit ($Z = \sigma S^2/\kappa$). As shown in Fig. 1.3, the maximum value of the power factor is at around 10^{20} cm^{-3} . Thus, we design the heavily doped semiconductors for thermoelectric materials, which have the carrier concentration from 10^{19} to 10^{20} cm^{-3} . However, as shown in the previous subsection, the heavy fermion compounds and Co oxides have the large Seebeck coefficient in spite of the metallic state, and then the search for the thermoelectric material has recently been spread in various materials.

1.3 Narrow-gap semiconductor FeSb₂

1.3.1 Huge Seebeck coefficient of FeSb₂

A huge Seebeck coefficient, $S \sim -45 \text{ mV/K}$ at 10 K, was observed in a narrow gap semiconductor of FeSb₂ as shown in Fig. 1.4.[16] This huge value cannot be explained by the conventional model. In non-degenerate semiconductors, the Seebeck coefficient is simply related to an energy gap Δ : $S = \frac{k_B}{e}(\frac{\Delta}{k_B T} - r)$, where the r is scattering parameter.[23] To observed the huge value of -45 mV/K at 10 K, the energy gap Δ becomes about 5000 K, meaning an unrealistic situation, in which the carrier concentration becomes almost zero (Fig. 1.3). On the other hand, in the case of the degenerate (metallic) model, the Seebeck coefficient is described by $S = \frac{\pi^2 k_B^2 T}{3e\epsilon_F}(r + \frac{3}{2})$, where we assume the 3-dimensional non-interacting Fermi gas.[24] This model can be valid when $\epsilon_F > k_B T$ is satisfied. For this reason, the upper limit of S with this model is estimated about $850 \mu\text{V/K}$. Thus, we cannot understand the origin of this huge Seebeck coefficient with the conventional theory.

To explain the huge Seebeck coefficient for FeSb₂, Sun *et al.* proposed that the huge Seebeck coefficient is observed due to an unique band structure of strongly electron correlated semiconductors, such as Kondo insulators.[18, 25, 26] The Kondo insulators have a small hybridization gap with a narrow distribution of the electronic density of states close to the Fermi level for the mixing of broad conduction bands with narrow d - or f -bands (Fig. 1.5(a)).[30] This band structure yields a steep variation of the density of states near the Fermi level, and then the large Seebeck coefficient is theoretically expected, since the Seebeck coefficient is proportional to the energy derivatives of the density of states as described in Eq. (1.20) (Fig. 1.5(b)). A typical Kondo insulator of Ce₃Pt₃Sb₄ shows a large Seebeck coefficient ($\sim 350 \mu\text{V/K}$) at low temperature (Fig. 1.6).[14] A narrow gap semiconductor FeSi, which is considered as a $3d$ -orbital Kondo insulator,

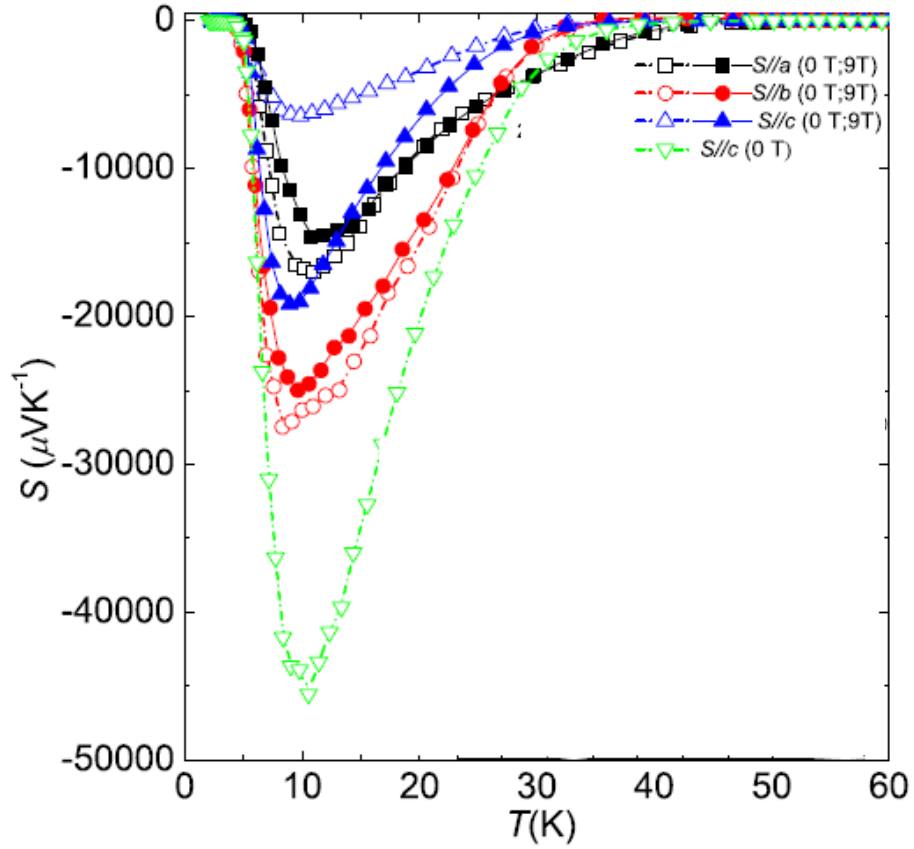


Figure 1.4: The Seebeck coefficient of FeSb₂ single crystal as a function of temperature measured in magnetic fields of 0 T (data points with dotted curves) and 9 T (solid curves), applied along the *a*-axis (black square), *b*-axis (red circle) and *c*-axis (blue and green triangles).[16]

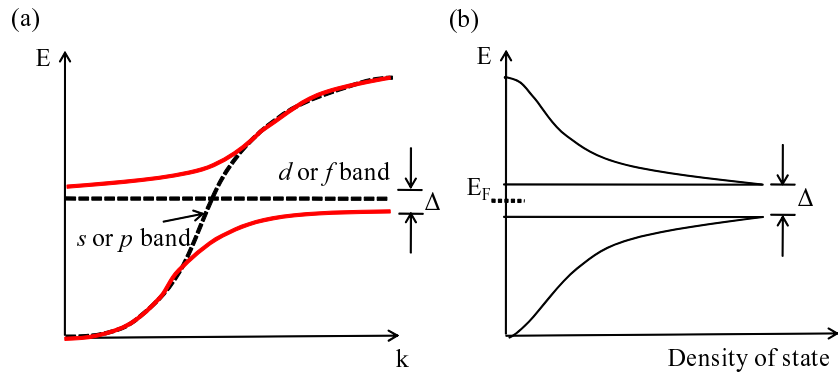


Figure 1.5: (a) A schematic picture of a band distribution for the Kondo insulator. (b) The density of states for the Kondo insulator.

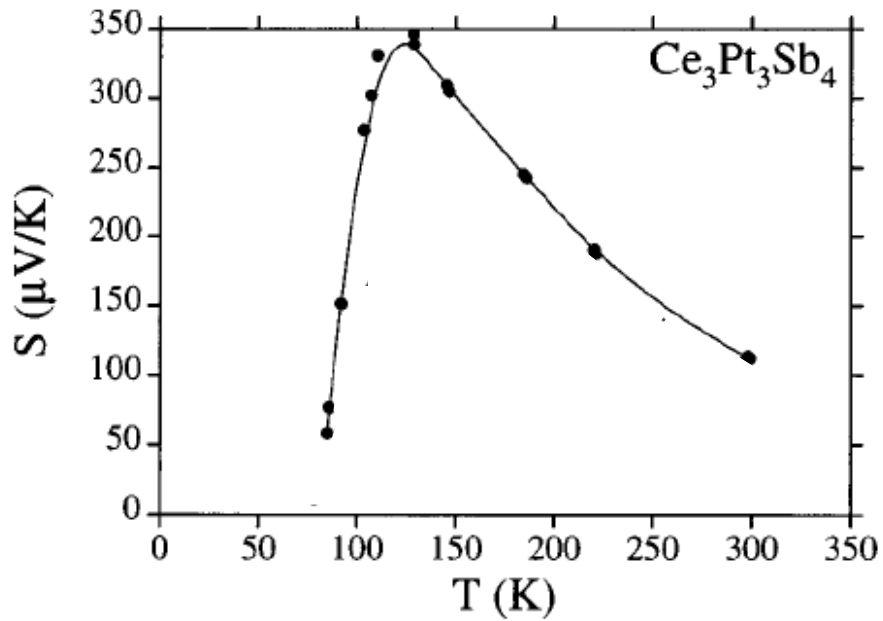


Figure 1.6: The temperature dependence of the Seebeck coefficient for $\text{Ce}_3\text{Pt}_3\text{Sb}_4$. [14]

also has a large Seebeck coefficient ($|S| \sim 500 \mu\text{V/K}$) around 100 K.[31, 32] However, the absolute value of the Seebeck coefficient observed in FeSb_2 is much larger than that of Kondo insulators, suggesting another novel effects.

Due to the huge Seebeck coefficient, the large thermoelectric efficiency is expected in this compound. Actually, the largest power factor $PF \sim 2300 \mu\text{WK}^{-2}\text{cm}^{-1}$ is observed, which is 65 times larger than that of Bi_2Te_3 -based thermoelectric materials.[16] This large power factor suggests that this compound has a potential as the Peliter refrigerator at low temperature. However, the thermoelectric efficiency ($ZT = \sigma S^2 T / \kappa$; dimensionless figure of merit) remains small because of a large thermal conductivity of $\sim 350 \text{ W/mK}$ at 15 K.

Figure 1.7 shows the temperature dependence of the $\text{FeSb}_{2-x}\text{Sn}_x$ for polycrystalline samples.[17] The sample for $x = 0$ has the maximum value of $|S| \sim 500 \mu\text{V/K}$ at 30 K, which is two order of magnitude smaller than that of single crystals. Generally, single crystal and polycrystalline samples tend to have the same value of S , because the value of the Seebeck coefficient is not sensitive to an extrinsic scattering due to the crystal boundary. Moreover, a large sample dependence of S is reported,[18] implying that the huge Seebeck coefficient is strongly affected by the non-stoichiometry and impurity.[26] To clarify the origin of the large Seebeck coefficient, we need systematic studies with samples which show the large Seebeck coefficient.

1.3.2 Crystal structure of FeSb_2

The narrow-gap semiconductor FeSb_2 crystallizes in a marcasite structure with the space group $Pn\bar{n}m$ as shown in Fig. 1.8.[27] The lattice constants are $a = 5.83 \text{ \AA}$ and $b = 6.54 \text{ \AA}$ and $c = 3.20 \text{ \AA}$ at room temperature. FeSb_6 octahedra share the edges along the c -axis, and the corners along the a - and b -axes. The FeSb_6 octahedron has two different Fe-Sb bond lengths: The longer one (solid line in Fig. 1.8) is about 2.60 \AA and the shorter one (dotted line in Fig. 1.8) is about 2.57 \AA at room temperature.

The marcasite structure has two distinguished forms, which are characterized by a cation-anion-cation angle α parallel to the orthorombic c -axis, shown in Fig. 1.9.[28] The regular marcasite has an angle $\alpha < 90^\circ$, and anomalous marchasite has a angle $\alpha > 90^\circ$. These two structures have different carrier numbers n in $3d$ state, the former is $n \leq 4$ and the latter is $n \geq 4$. FeSb_2 belongs to the regular marcasite structure with $\alpha \simeq 76^\circ$ at room temperature, having the Fe^{4+} ($3d^4$) electron configuration.[28]

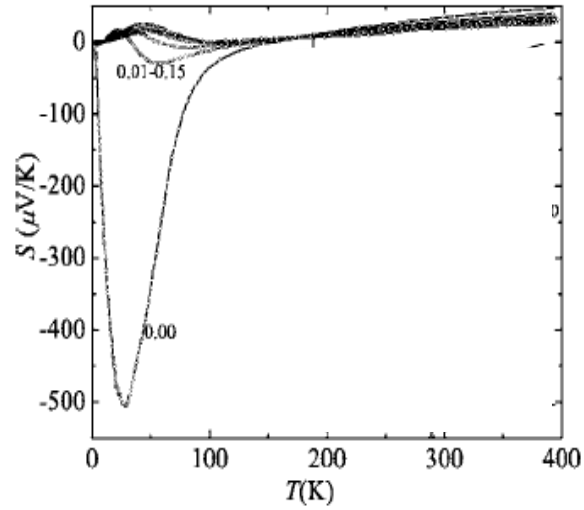


Figure 1.7: The temperature dependence of the Seebeck coefficient for polycrystals of $\text{FeSb}_{2-x}\text{Sn}_x$. [17]

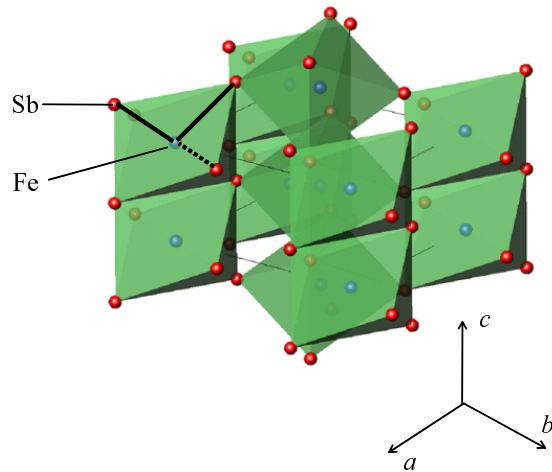


Figure 1.8: The crystal structure of FeSb_2 . Blue and red atoms are Fe and Sb, respectively. The unit cell is orthorhombic and the structure belongs to the space group of No. 58 ($Pn\bar{m}$).

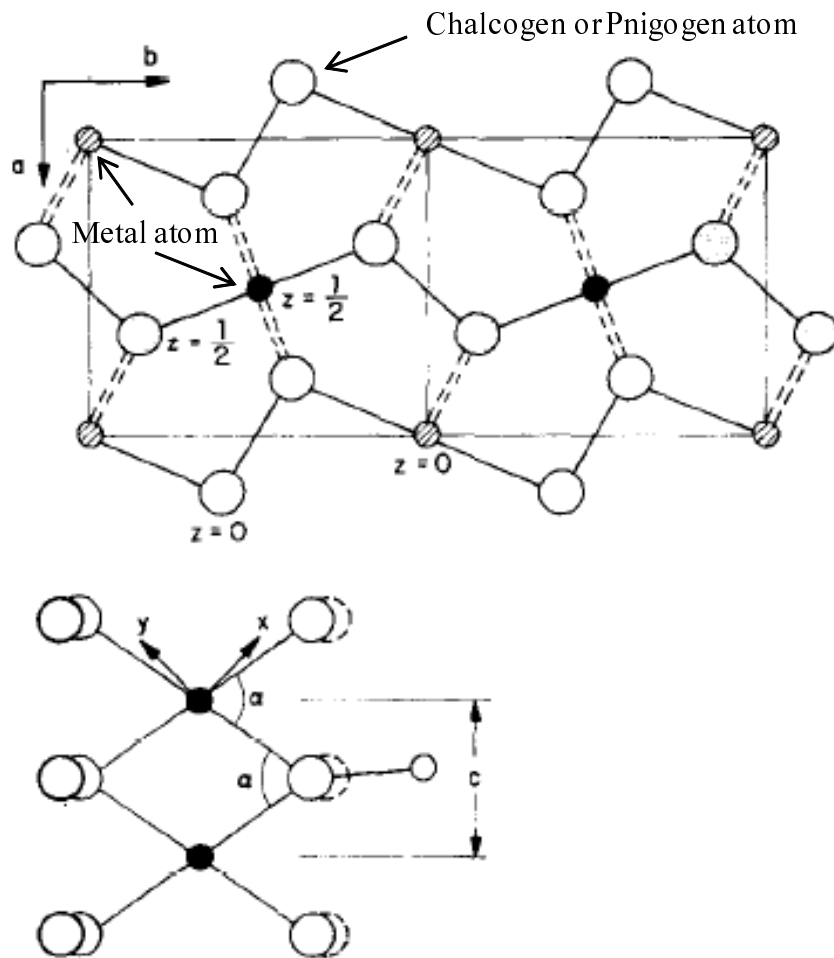


Figure 1.9: The orthorhombic marcasite structure. The upper and lower figures show the ab plane and the c -axis chain, respectively.

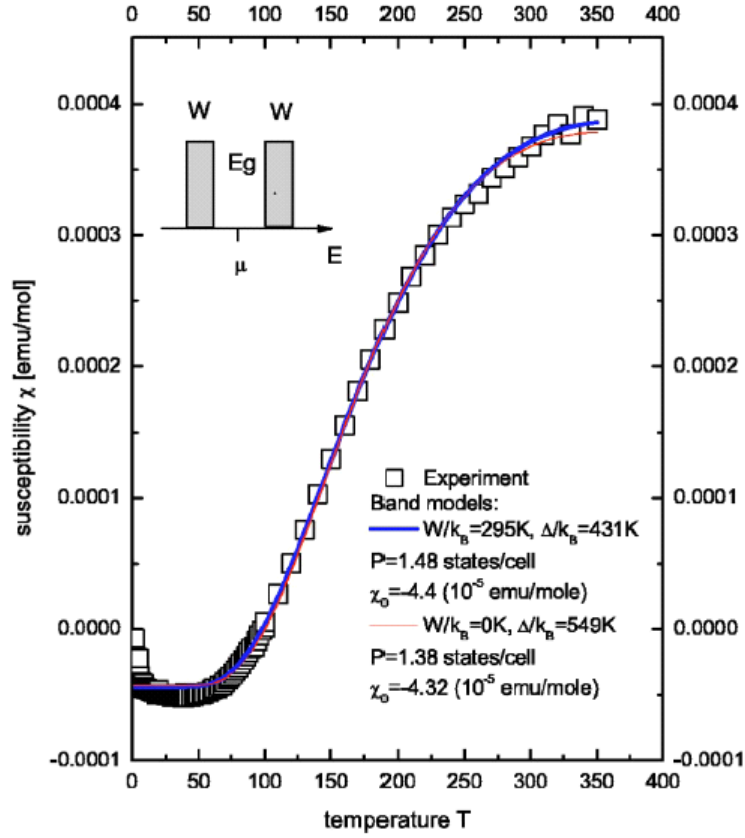


Figure 1.10: The magnetic susceptibility of FeSb_2 . Solid curves are fitting results using the model density of states shown in the inset.[27, 29]

1.3.3 Magnetic property

Figure 1.10 shows the temperature dependence of the magnetic susceptibility χ for the single crystal FeSb_2 . [27, 29] χ has a temperature independent diamagnetic behavior below 50 K, the value of which is -4×10^{-5} emu/mol (close to the core diamagnetic value of -4.7×10^{-5}), and shows a diamagnetic to paramagnetic crossover around 100 K. In the Kondo insulator, the localized d or f electron bands are hybridized with conduction bands, which make the energy gap at the Fermi energy with a very large peak in the density of states at the gap edge. At low temperature, all carriers are in the bands below the Fermi energy, realizing a non-magnetic state, while at high-temperature, the carriers are excited to the band above the Fermi energy, inducing the magnetic moment. This temperature induced crossover has been analyzed with a model of two narrow bands (peaks)

at the density of states, in which the bands are separated by E_g , and have a band width of W , as shown in inset Fig. 1.10. This model has been successfully applied to show the validity of a picture with the Kondo insulator on the thermodynamics of FeSi.[33]

The Pauli susceptibility of an itinerant electron system with the density of states $D(E)$ is described as

$$\chi(T) = -2\mu_B^2 \int_{c\text{-band}} D(E) \frac{\partial f(E, \mu, T)}{\partial E} dE, \quad (1.27)$$

where μ_B is the Bohr magneton and $f(E, \mu, T) = (\exp[(e - \mu)/k_B] + 1)^{-1}$. The factor 2 in the above equation is due to the contribution from the holes in the valence band and electrons in the conduction band. Assuming $D(E) = Np/W$ and $\mu = W + \Delta$, the magnetic susceptibility is obtained by

$$\chi(T) = -2\mu_B^2 \frac{Np \exp(\beta\Delta)(1 - \exp(\beta W))}{W(1 + \exp(\beta\Delta))(1 + \exp(\beta(\Delta + W)))} + \chi_0, \quad (1.28)$$

where p is the number of states/cell, and N is the number of unit cells. From the fitting result, we obtain reasonable values for parameters: $0 \text{ K} < W/k_B < 400 \text{ K}$ and $850 \text{ K} < E_g/k_B < 1100 \text{ K}$, which are comparable to parameter values obtained for FeSi.[33]

1.3.4 Resistivity and Hall coefficient

Figure 1.11 displays the temperature dependence of the resistivity for the single crystal FeSb₂ along the a , b , and c axes in magnetic fields of 0 T and 9 T, where the magnetic field is parallel to the current direction.[16] The resistivity increases with decreasing temperature like semiconductors from 300 to 30 K in all directions and a ‘‘shoulder’’ exists from 30 to 10 K. Below 5 K, the resistivity of all directions shows a weak temperature dependence. The upper inset of Fig. 1.11 presents an Arrhenius plot of $\rho(T)$, from which three distinct energy scales can be derived. The weak temperature dependence at lowest temperature is probably due to extrinsic impurity states. In the temperature from 5 to 15 K, the energy gap of $\Delta \sim 6 \text{ meV}$ is evaluated, whereas in the temperature range 50 to 300 K the Arrhenius plot leads to the energy gap of $\Delta \sim 30 \text{ meV}$ using an activation function $\rho \propto \exp(\Delta/2k_B T)$.

The temperature dependence of the Hall coefficient R_H is shown in Fig. 1.12.[34] $R_H(T)$ is negative in the whole temperature range, indicating that the transport properties are dominated by electrons. A dramatic increase of R_H with decreasing temperature is observed from 100 to 30 K, which can be explained by the carrier excitation due to the band gap. Below 30 K, the slope becomes weak,

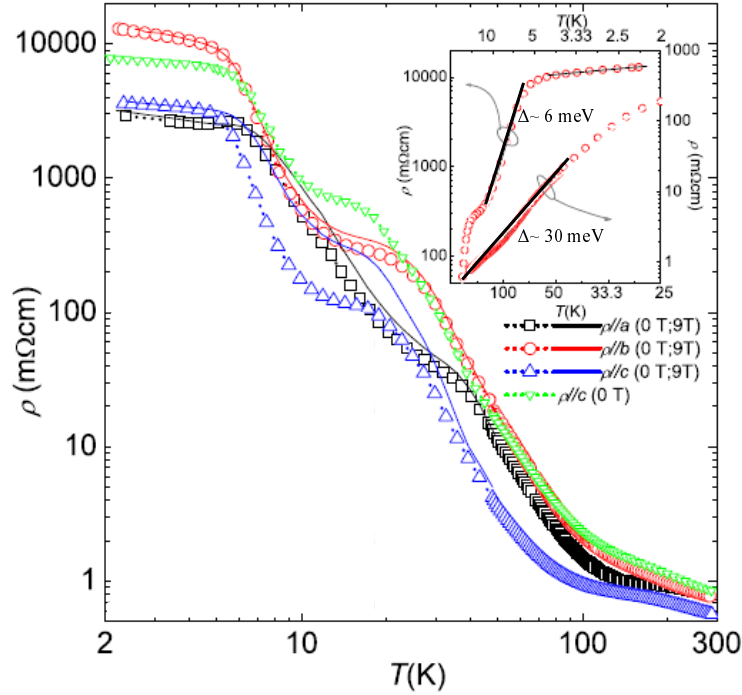


Figure 1.11: The electrical resistivity as a function of temperature measured in magnetic fields of 0 T (data points with dotted curves) and 9 T (solid curves), applied along the a -axis (black square), b -axis (red circle) and c -axis (blue and green triangles). The inset is an Arrhenius plot of the resistivity. The energy gaps are evaluated by the linear fitting with an activation function $\rho \propto \exp(\Delta/2k_B T)$. [16]

which may correspond to the shoulder and the small energy gap observed in ρ . The decrease of $|R_H(T)|$ below 7 K may be associated with the saturation of $\rho(T)$, implying the existence of the in-gap state. These transport and the magnetic properties suggest that this compound is a semiconductor with two small energy gaps, which may be formed by the Kondo interaction.

1.3.5 Band structure calculation

From the crystal structure, Goodenough proposed a quantitative band structure of the marcasite compounds. [28] First, the d -orbitals of transition metal ions surrounded by chalcogen or pnictogen ions with the octahedral configuration are split into t_{2g} and e_g orbitals due to the crystal fields. Then, the t_{2g} orbitals in marcasite structure is split into the higher d_{xy} orbital, which is directed toward near-neighbor cations along the c -axis, and the lower two-fold d_{yz} and d_{zx} orbitals (Fig. 1.13(a)).

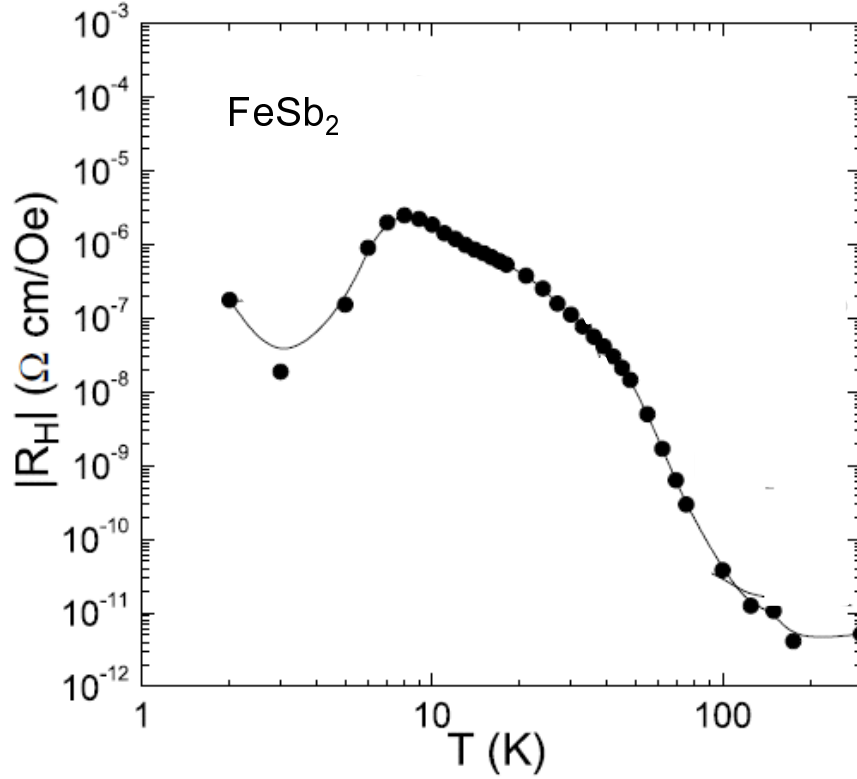


Figure 1.12: The Hall coefficient of the FeSb₂ single crystal.[34]

In this model, x and y axes are along to the c -axis direction as shown in Fig. 1.9, and the energy levels are determined by the c -direction X-Fe-X angle α (X is the chalcogen or pnigogen ions). From this model, a band structure of FeAs₂, which has the regular marcasite structure ($\alpha \sim 72.5^\circ$), is proposed, as shown in Fig. 1.13(b). Considering this structure, it is realized that the d_{xy} orbital is not orthogonal to the σ -bonding anion orbitals, while the d_{yz} and d_{zx} are nearly orthogonal. In this case, the local d_{yz} and d_{zx} band lie below the Fermi energy, and the hybridization bands between Fe d_{xy} (and e_g) and As $4p$ states exist above the Fermi energy. These local d bands and the hybridized bands make a small energy gap in this compound.

Above analysis predicts that a small energy gap is formed in FeSb₂ due to the hybridization between Fe d and Sb p orbitals. Recently, some groups reported band calculations for FeSb₂. [17, 35] Bientien *et al.* performed the band calculation with the full potential linearized augmented plane wave plus the local orbital (LAPW+lo) method as implemented in the WIEN2k code. [17] The calculated re-

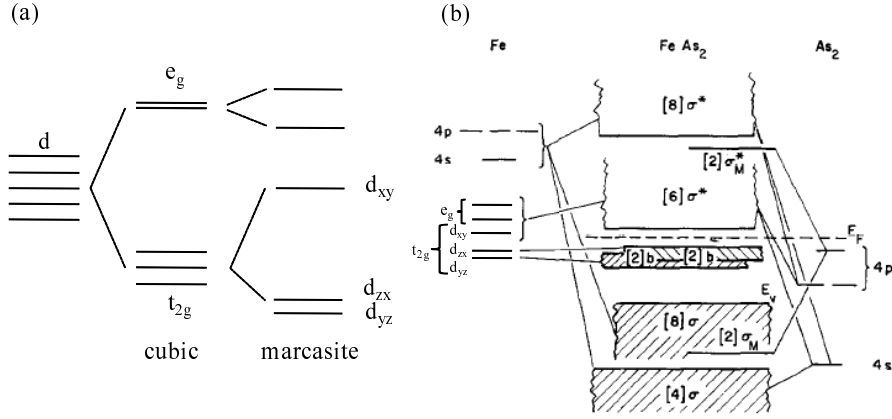


Figure 1.13: (a) Orbital states of the marchasite structure. (b) The schematic band structure of FeAs₂. [28]

sult is shown in Fig. 1.14. The contribution of each orbitals to the density of states is displayed in Fig. 1.14(b). In this calculation, the z -axis is taken along a short Fe-Sb bond ($\sim 2.57 \text{ \AA}$) directed to the c -axis, and the x and y axes are along longer Fe-Sb bonds ($\sim 2.60 \text{ \AA}$). Although the orbitals of d_{z^2} and $d_{x^2-y^2}$ are usually destabilized in an ionic crystal field, these orbitals are stabilized due to the hybridization effect between Fe d and Sb p orbitals, as shown in Fig. 1.14(b). The band structure shows the existence of the narrow energy gap and the large density of states at the slightly below and above the Fermi energy, which is thought as the origin of the large Seebeck coefficient of FeSb₂. However, this calculation result suggests a metallic ground state, which has a nonzero value of the density of states $D(\epsilon_F)$ at the Fermi energy as shown in the inset of Fig. 1.14(a). To reproduce the insulating state, Tomczak *et al.* modifies the band structure using the GW approximation, which can include the dynamical effects of electronic correlations. [35] Figure 1.15(a) shows the band calculation result of the Local density approximation (LDA) and GW approximation. The metallic state calculated with LDA is changed to the insulating state in the GW approximation. The insulating state of FeSb₂ is possibly explained by above analysis, while the important problem about the Seebeck coefficient remained open. The huge value of the Seebeck coefficient is not reproduced from the above band structure. Tomczak *et al.* calculated the Seebeck coefficient using the above band model based on the Kubo formula, showing the crucial deviation from experimental data below 30 K, as shown in Fig. 1.15(b). In addition, the two gap state observed in transport properties has not been explained by the band calculation studies, and the gap formation mechanism has not been unrevealed.

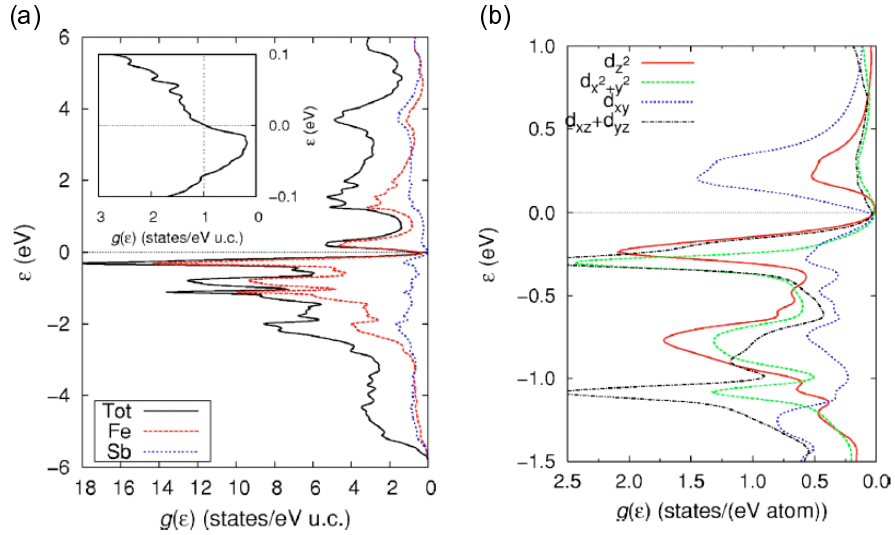


Figure 1.14: (a) The density of states for FeSb_2 . The inset figure shows the density of states near the Fermi energy. (b) Detail contributions of each Fe d -orbitals to the density of states.

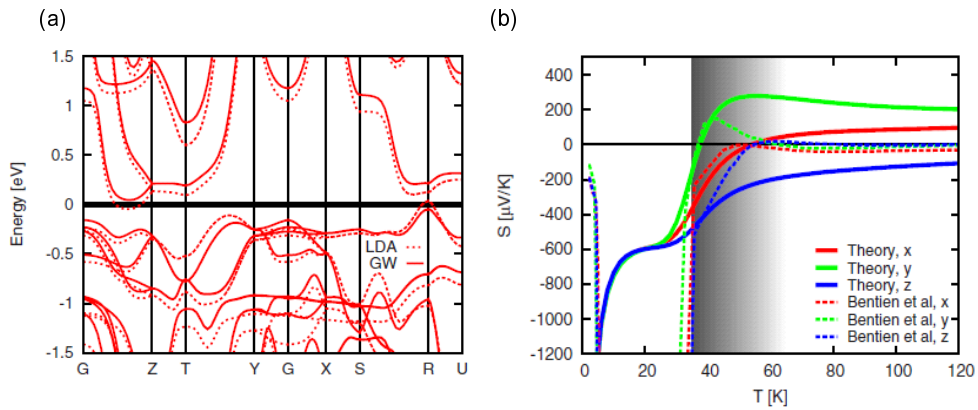


Figure 1.15: (a) The band structures of FeSb_2 with the GW approximation and LDA. (b) The Seebeck coefficient calculated by Tomaczak *et al.* with the band calculation result, depicted by solid curves. The dotted lines are experimental results of Bentien *et al.*

Chapter 2

Ppm-level impurity effect of transport properties on single crystal

2.1 Introduction

In this chapter, we show a ppm-level impurity effect of physical properties for the narrow gap semiconductor FeSb₂. Extensive studies have been conducted to clarify the origin of the huge Seebeck coefficient (~ -45 mV/K) since its discovery.[16, 25, 26, 18] However, some groups reported a large sample dependence of the Seebeck coefficient.[16, 17, 26] For example, a much smaller value of $S \sim -500$ μ V/K was observed for polycrystalline samples, and this may indicate that physical properties of FeSb₂ are highly sensitive to impurities and/or nonstoichiometries. Thus, to make clear the origin of the large sample dependence of physical properties, we grow the single crystals from metal powders of different purity to systematically control the sample purity, and measure the magnetic and the transport properties.

2.2 Experiment

2.2.1 Sample preparation method

The single crystals of FeSb₂ were grown by a self-flux method.[16] High-purity metal powders of Fe 0.948 g and Sb 24.041 g (Fe : Sb= 8 : 92) were mixed in an alumina crucible, and sealed in an evacuated silica tube (Fig. 2.1(a)). The tube was heated up to 1050 °C at a rate of 200 °C/h, kept at this temperature for 2h, cooled to 775 °C at a rate of 20 °C/h, and slowly cooled to 640 °C at a rate of 9

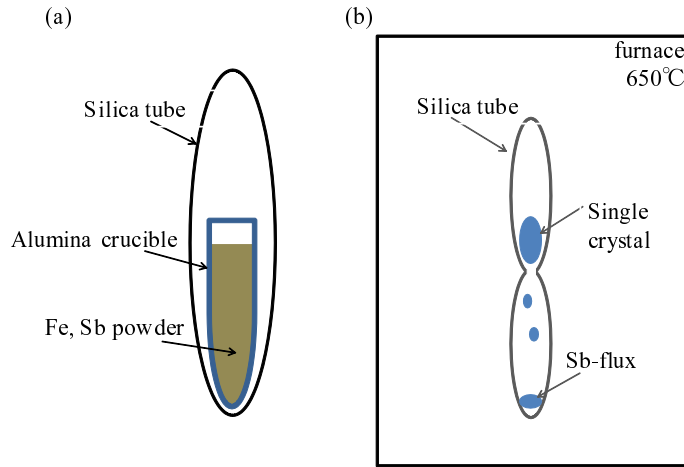


Figure 2.1: (a) A schematic picture of the sample growth method with an evacuated silica tube. The Sb and Fe powders are in the alumina crucible and sealed in an evacuated silica tube. (b) The elimination method of Sb-flux.

°C/h. Then, the crystals were taken out of the silica tube, and put at one side of an evacuated silica tube, the middle part of which was narrow. The Sb flux was dripped to the other side of the tube by annealing at 650 °C for 10 h (Fig. 2.1(b)).

We prepared four kinds of single crystals with different purities. The crystal called 5N/6N was grown from 99.999% (5N) pure Fe powder and 99.9999 % (6N) pure Sb powder. The second one called 3N/3N was grown from 99.9 % (3N) pure Fe and Sb. The other two samples called 5N/3N and 3N/6N have similar meanings. From this preparation method, we can control the impurity level from 0.0001 to 0.1 %.

X-ray diffraction patterns were measured for single crystals pulverized from part of the crystal, where a small amount of Sb was detected. This excess Sb was eliminated with nitric acid. Figure 2.2 shows a photographic image of a typical single crystal which is about $3 \times 3 \times 3 \text{ mm}^3$.

2.2.2 Experimental methods of the magnetic susceptibility and transport properties

The magnetic susceptibility was measured using the Quantum Design Magnetic Property Measurement System (MPMS) with a magnetic field of 10 kOe from 5 to 300 K. We measured samples which are smaller than $2 \times 2 \times 2 \text{ mm}^3$.

The electrical resistivity was measured with a four-terminal method from 300 to 5 K by a nanovolt meter (Agilent 34420A) and a current generator (ADVAN-



Figure 2.2: The photographic image of a typical single crystal of FeSb₂. One division is 1 mm in the diagram.

TEST R6142). The temperature is determined with a Cernox Resistor (Lake Shore) by a multimeter (Agilent 34401A). The Hall coefficient was measured under a magnetic field H of 10 kOe using the Quantum Design Physical Property Measurement System (PPMS). Here, we measured the Hall voltage V_H , rotating the sample from 0° to 180° for the external field to eliminate the background voltage V_{BG} by this equation;

$$V_H = \frac{(V_H^{0^\circ} + V_{BG}) - (V_H^{180^\circ} + V_{BG})}{2} = \frac{V_H^{0^\circ} - V_H^{180^\circ}}{2}. \quad (2.1)$$

The Seebeck coefficient was measured using a steady-state technique from 5 to 300 K, as shown in Fig. 2.3. We applied the temperature different about 1 K between both ends with a strain gage. The temperature gradient was measured using the differential thermocouple of the constantan wire. We prepared a polished thin sample with a cross section of $0.1 \times 0.02 \text{ mm}^2$ to measure the Seebeck coefficient because it is difficult to make the temperature gradient in the sample due to a large thermal conductivity (the maximum value is $\sim 350 \text{ W/mK}$ at 15 K) at low temperature.[16]

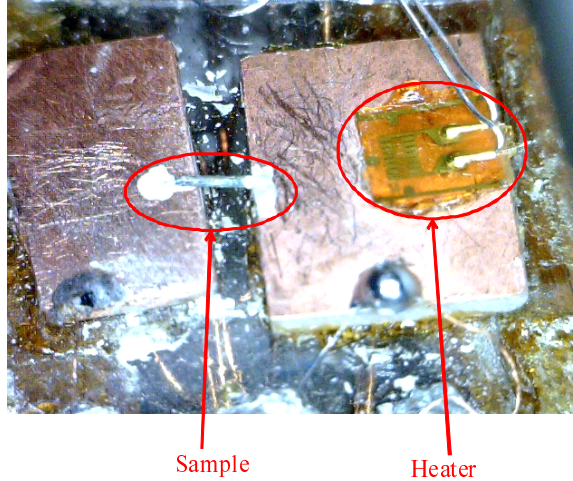


Figure 2.3: The measurement system of the Seebeck coefficient with a steady-state technique. The sample was polished into a thin bar which thickness is less than 0.1 mm.

2.3 Result and Discussion

2.3.1 Magnetic susceptibility

The temperature dependence of the magnetic susceptibility χ is shown in Fig. 2.4. From 50 K, this value increases with increasing temperature, which has been understood as a paramagnetism of thermally activated carriers with narrow bands, as explained in Section 1.3.3.[27] The susceptibility of the 3N/3N and 5N/3N samples shows an upturn with decreasing temperature below 50 K, indicating the presence of a small amount of the magnetic moment. Assuming that the impurity density is 0.1 %, we evaluate the effective spin number of the 3N/3N sample to be $S \sim 1.7$ using the Curie law, which is consistent with the magnetic moment of Fe. Although we cannot specify the origin of the magnetic moment at present, it is clear that the Sb impurity determines the magnetic properties of FeSb₂ crystals.

2.3.2 Electrical resistivity

Figure 2.5 presents the temperature dependence of the resistivity ρ for the four samples below 100 K. All the $\rho - T$ curves merge above 40 K, which obey the thermally-activated transport with an activation energy of ~ 30 meV evaluated

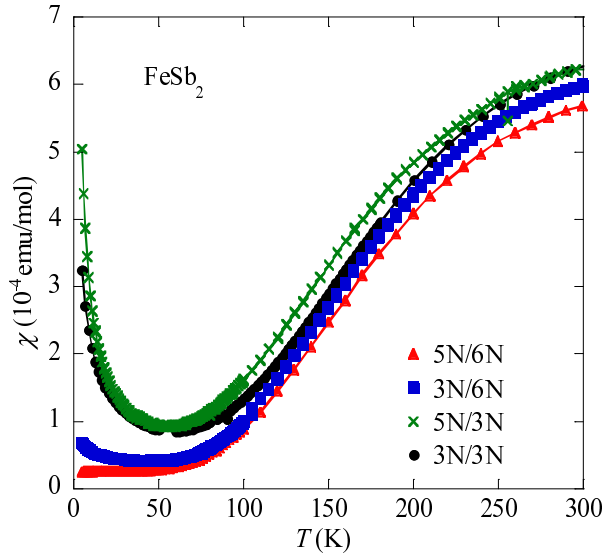


Figure 2.4: The temperature dependence of the magnetic susceptibility for all samples. The magnetic susceptibility increases with increasing temperature above 50 K, which can be understood as a paramagnetism of thermally activated carriers.

from the Arrhenius plot, as shown in the inset of Fig. 2.5. Below 40 K, on the other hand, ρ starts to deviate from the activation transport. In particular, ρ of the 5N/6N sample exhibits a plateau from 10 to 20 K, as already reported in Ref. 16. The 3N/6N sample shows almost the same ρ as the 5N/6N sample, but the plateau is somewhat smeared. Below 10 K, ρ of the 5N/6N and 3N/6N data again increases with decreasing temperature, possibly suggesting the presence of the smaller energy gap, which is already reported by Ref. 6.

2.3.3 Hall coefficient

Figure 2.6 shows the Hall coefficient R_H as a function of temperature below 100 K. R_H of the 3N/3N and 5N/3N samples is negative, and $|R_H|$ increases with decreasing temperature. On the other hand, R_H of the 5N/6N sample changes its sign from positive above 45 K to negative below 45 K. We emphasize that $|R_H|$ of the 5N/6N sample rapidly increases with decreasing temperature by about four orders of magnitude (from $5.2 \times 10^{-1} \text{ cm}^3/\text{C}$ at 40 K to $2.5 \times 10^{-1} \text{ cm}^3/\text{C}$). R_H of the 3N/6N sample behaves similar to the 5N/6N sample, but the sign remains negative above 100 K.

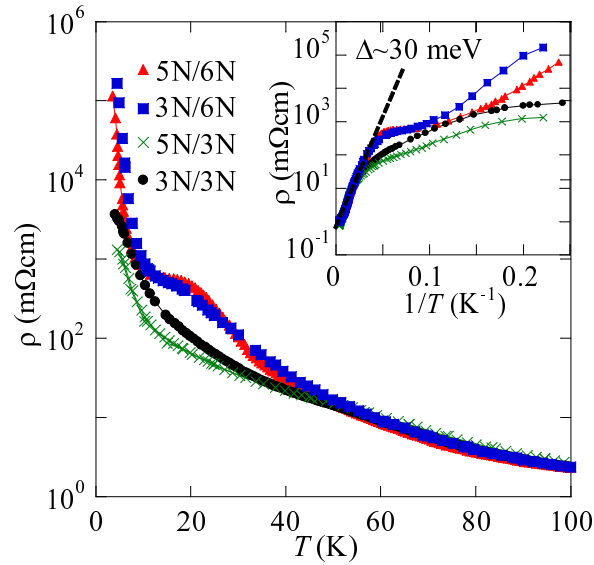


Figure 2.5: The electrical resistivity below 100 K. Inset shows the Arrhenius plot, from which we evaluate the activation energy by a thermal activation function $\rho \propto \exp(\Delta/2k_B T)$ above 100 K.

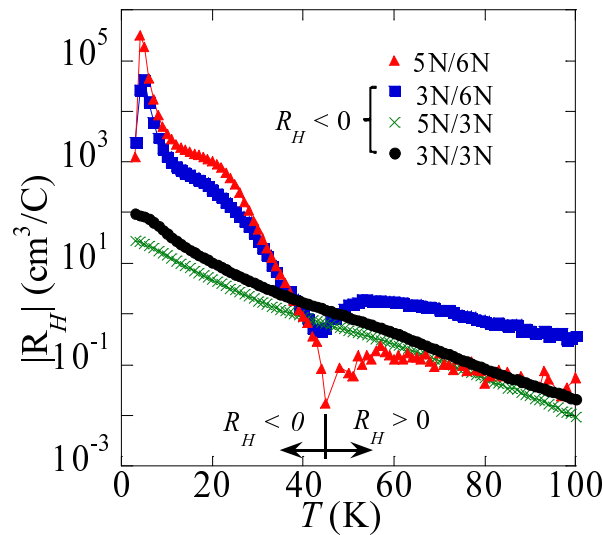


Figure 2.6: The temperature dependence of the Hall coefficient of single crystals between 0 and 100 K. The sign of the Hall coefficient of the 5N/6N sample changes at about 45 K, while that of the other samples does not change.

2.3.4 Carrier concentration and mobility

Let us discuss the carrier density n and the Hall mobility μ_H , in the framework of a single band model. Clearly, FeSb₂ is a multi-band conductor, because the Hall coefficient of the 5N/6N sample exhibits the sign change. However, we may use an expression for a single carrier system with a parabolic band below 40 K, where the magnitude of R_H is larger than 10^{-1} cm³/C. Note that the magnitude of R_H in a multi-band conductor is smaller than the magnitude of R_H calculated from each single-band components. Thus, $n = 1/eR_H$ gives the upper limit of the carrier density, and $\mu_H = R_H/\rho$ gives the lower limit of the Hall mobility.

Figure 2.7(a) and 2.7(b) show the carrier density n and the Hall mobility μ_H , respectively. The 5N/6N and 3N/6N samples have much smaller values of carrier concentrations than those of the 3N/3N and 5N/3N samples below 35 K. This suggests that an energy gap is opened at the chemical potential in the 5N/6N and 3N/6N samples, while the gap is somewhat off the chemical potential in the 3N/3N and 5N/3N samples. In other words, impurities in the Sb powder effectively act as dopants to supply electrons. The carrier density of 5N/3N and 3N/3N samples is of the order of 0.01 % per unit cell, which is consistent with the purity of 3N. Here, we emphasize that n of the 5N/6N and 3N/6N at 20 K is supplied from ppm-level imperfections. Such an extremely low carrier density at 20 K is the main reason why FeSb₂ is highly sensitive to purity. According to chemical analysis of the 3N Sb powder, Pb(0.03%), Zn (0.01 %) and As (0.005 %) are major impurity elements. Sun *et al.* reported that the As substitution effectively acts as carrier-doping, although this is isovalent substitution.[18] Accordingly, we can understand why the 5N/3N and 3N/3N samples have larger carrier density. On the other hand, we cannot understand why impurities in the Fe powder (Ni 0.008 %, Co 0.004 % and Mn 0.001 %) hardly affected the physical properties. One possibility is that the flux growth may exclude such impurities spontaneously.

As shown in Fig. 2.7(b), the carrier mobility of 3N/3N weakly depends on temperature like some conventional semiconductors. In contrast, the mobility of 5N/6N samples substantially increases with decreasing temperature. The carrier mobility enhancement at low temperature in high-quality FeSb₂ crystals is also reported by other groups.[18, 27] This enhancement may be a piece of the evidence for the strong electron-electron correlation; The scattering rate $1/\tau$ is expected to be strongly reduced with n , when the carrier-carrier scattering is dominant.[36, 37] On the other hand, another possibility is considered that FeSb₂ is as pure as high-quality Ge, where $\mu_H \propto T^{-3/2}$ due to the reduction of thermal scattering, which is visible down to 10 K.[38] To clarify the origin of the strong temperature dependence of the mobility, we need more detailed experiments, since the mobility was evaluated here based on the single carrier model, while this material is intrinsically a multi-band system.

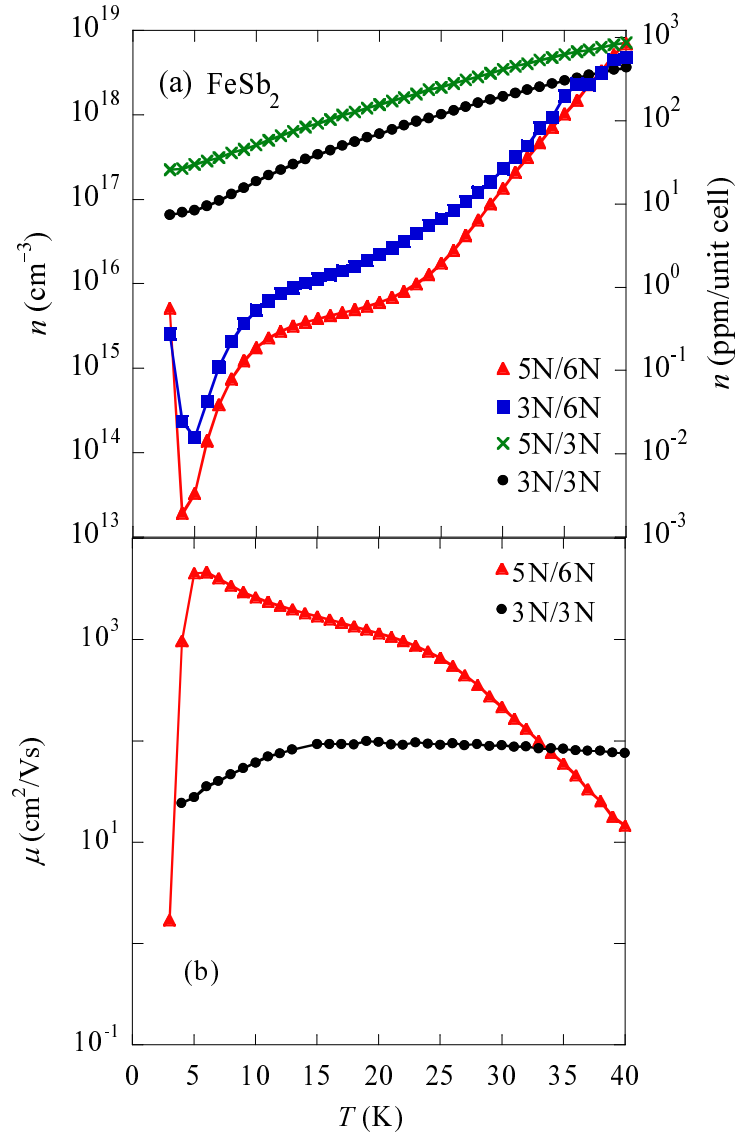


Figure 2.7: (a) The carrier concentration evaluated with the single band model ($n = 1/R_{He}$). The left and right axes show the unit of cm^{-3} and ppm/unit cell, respectively. (b) The carrier mobility of 5N/6N and 3N/3N samples.

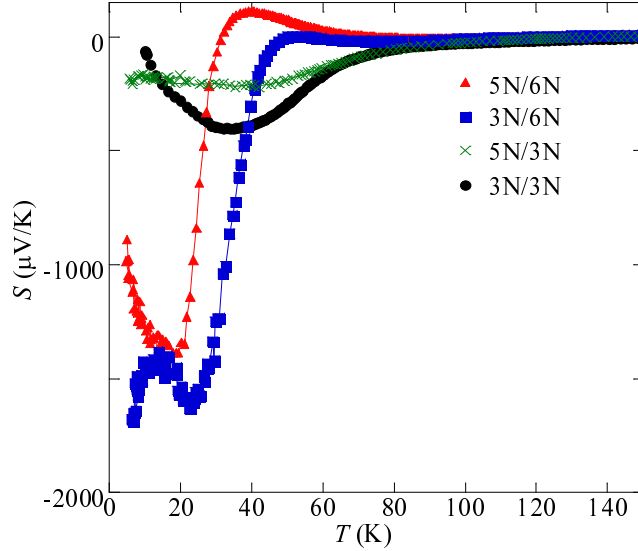


Figure 2.8: (a) The Seebeck coefficient of single crystals of FeSb_2 below 100 K. 5N/6N and 3N/6N samples have large peaks of $|S|$ at around 20 K, while 3N/3N and 5N/3N samples show smaller peaks at around 35 K.

2.3.5 Seebeck coefficient

Figure 2.8 shows the Seebeck coefficient S in the temperature range from 5 to 150 K. Temperature dependence of S is clearly different between the 5N/6N and 3N/3N samples. $|S|$ of the 3N/3N samples increases rapidly with increasing temperature from 5 to 35 K and reaches a maximum of $400 \mu\text{V/K}$, and decreases from 35 to 150 K. This is essentially the same as that observed in polycrystalline samples.[17] In contrast, $|S|$ in the 5N/6N samples is much larger at lower temperature ($1500 \mu\text{V/K}$ at 20 K), and rapidly decreases to undergo a sign change near 40 K. We did not observe the colossal values of S reported in Ref. 16, the reason of which will be discussed later. The temperature dependence is complicated, and a second sign change happens near 70 K. $|S|$ of the 3N/6N and 5N/3N samples are almost the same as the 5N/6N and 3N/3N samples, respectively, indicating that the impurity in the Sb powder determines the gross feature of S .

Now, let us discuss the difference of S between the 5N/6N and 3N/3N samples in relation to n . Here, we apply two expressions for S , which are introduced in Chapter 1.[26] The one is based on a 3-dimensional single band model for the degenerate electron system given by[24]

$$S = \frac{\pi^2 k_B^2 T}{3e\epsilon_F} \left(r + \frac{3}{2} \right), \quad (2.2)$$

where

$$\epsilon_F = \frac{h^2}{2m^*} \left(\frac{3n}{8\pi} \right)^{2/3}. \quad (2.3)$$

The other is based on a nondegenerate model given by[15]

$$S = \pm \frac{k_B}{e} \left[\frac{\Delta}{k_B T} + \left(r + \frac{5}{2} \right) \right], \quad (2.4)$$

where

$$n = 2 \left(\frac{2\pi m^* k_B T}{h^2} \right)^{3/2} \exp \frac{\Delta}{k_B T}. \quad (2.5)$$

The factor r is the carrier scattering parameter, and takes $-1/2$ for an electron-phonon scattering and $3/2$ for an impurity scattering, which are usually used in the analysis for thermoelectric materials. In Fig. 2.9, S given by Eqs. (2.2) and (2.4) are shown by solid and dotted curves for the 5N/6N and 3N/3N samples respectively. Here, r is assumed to be $3/2$, and m^* is equal to the bare electron mass. The ratio of $k_B T$ to ϵ_F determines which model should be used. Equation (2.2) is valid for $\epsilon_F > k_B T$ and equation (2.4) is valid for $\epsilon_F < k_B T$. For the 3N/3N sample, $\epsilon_F > k_B T$ is satisfied at all the temperature, whereas for 5N/6N sample ϵ_F is smaller than $k_B T$ below 35 K. In fact, the data of the 3N/3N sample are roughly reproduced by the calculated curve of the degenerate model, and the data of the 5N/6N sample are roughly consistent with the calculation based on the nondegenerate model below 35 K as shown in Fig. 2.9. This strongly suggests that the magnitude of S is explained by the carrier density. However, we have used the carrier concentration evaluated from the single band model, and then we need more precise method to obtain the carrier concentration by considering a multi-band feature for the 5N/6N sample.

Next we compare the 5N/6N sample with the huge-Seebeck-coefficient sample in Ref. 16. Equation (2.4) gives infinitesimally small carrier concentration for $S = -45$ mV/K at 10 K, which implies that some other unusual effects such as a phonon drag may occur. Phonon drag is a nonequilibrium phenomenon in a clean system,[39, 40, 41] and thus a purer sample may have a larger S . The detail discussion about the origin of the huge Seebeck coefficient is proposed in Chapter 4.

2.3.6 Power factor

Finally, we discuss the power factor of this material, which is a parameter to determine the efficiency for thermoelectric materials. The power factor PF is described as $PF = \sigma S^2$, which is numerator of the figure of merit $Z (= \frac{\sigma S^2}{\kappa})$. Due to the huge Seebeck coefficient at low temperature, Sun *et al.* reported a large power factor of $PF \sim 2300 \mu\text{WK}^{-2}\text{cm}^{-1}$ at 12 K, which value is 65 times larger

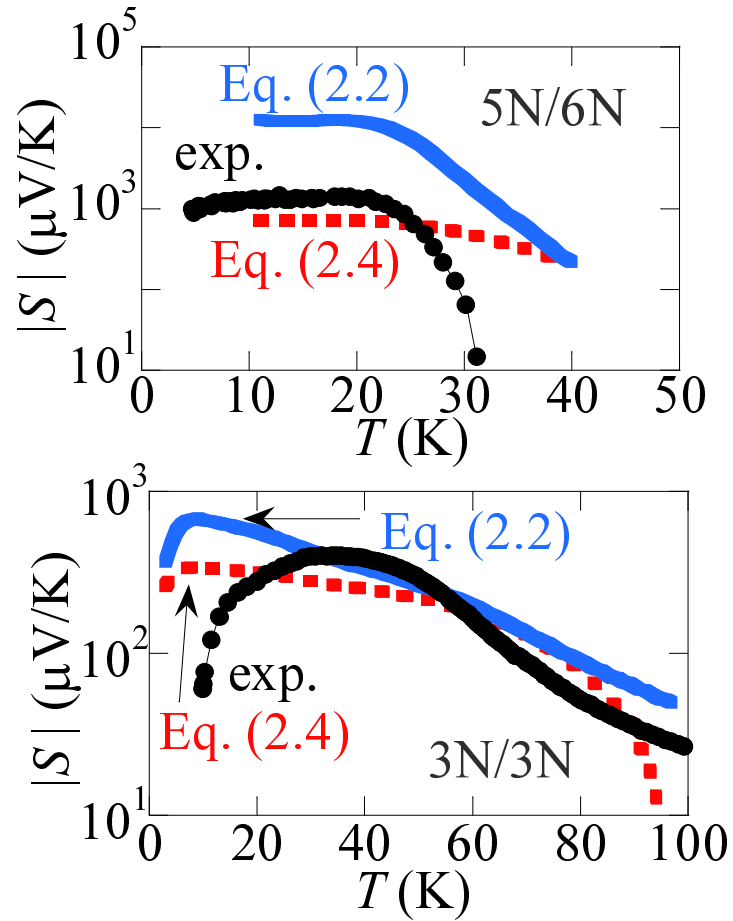


Figure 2.9: The Seebeck coefficient of the 5N/6N (the upper figure) and 3N/3N (the lower figure) samples. The curves of the blue solid line and red dotted line represent the results of the calculation for the degenerate (Eq. 2.2) and nondegenerate electrons (Eq. 2.4), respectively.

than that of a typical thermoelectric material Bi_2Te_3 . [16] Thus, this compound is expected as a Peltier device at low temperature. Another interesting feature of PF is observed in this compound. Figure 2.10 shows the carrier concentration dependence of PF for 5N/6N, 3N/3N, and the single crystal of Sun *et al.* [25] The peak positions are apparently different between 5N/6N and 3N/3N: The peak position of 5N/6N is at $n \sim 10^{16} \text{ cm}^{-3}$ and that of 3N/3N is at $n \sim 10^{19} \text{ cm}^{-3}$. In the conventional theory, the maximum of the power factor is realized at the carrier concentration of $\sim 10^{20} \text{ cm}^{-3}$ (Fig. 1.3), which is almost the same as the maximum position of PF for 3N/3N. In contrast, the maximum position of 5N/6N is significantly small, and a similar feature is seen in the crystal of Sun *et al.* To understand this unique properties, we need to remark the temperature dependence of the mobility in this compound. As shown in Fig. 2.7, the mobility of 3N/3N is almost constant in the whole temperature range, while the mobility of 5N/6N sample rapidly increases with decreasing temperature below 40 K. Thus, we think that the maximum positions at the low carrier concentration of 5N/6N and the sample of Sun *et al.* are realized due to the substantial increase of the mobility with decreasing temperature. However, the efficiency of FeSb_2 as the thermoelectric device is much small even in the sample of Sun *et al.*, which shows the significant large power factor, because of the high thermal conductivity ($\kappa \sim 350 \text{ W/mK}$ at 15 K). [16] For the improvement of this efficiency, we need to reduce the thermal conductivity, but in this compound, a small amount of impurities reduces the Seebeck coefficient and the carrier mobility, and then it is difficult to get the high efficiency in this compound.

2.4 Summary

We have prepared single crystals of FeSb_2 grown from metal powders of different purity. The susceptibility, resistivity, Hall coefficient and Seebeck coefficient have been drastically changed by a small amount of impurities in the Sb powder of the order of 0.1 % at low temperature. This is explained on the assumption that the impurities in the Sb powder used in the sample preparation effectively supply the conduction electrons. The dramatic change of S between the 5N/6N and 3N/3N samples at low temperature can be understood by the different value of n , and the large S of the 5N/6N sample at low temperature can be explained with the extremely small value of n . For the detailed analysis about the relation between the physical properties and the electronic structure, we conduct the study about magnetotransport properties shown in the next chapter.

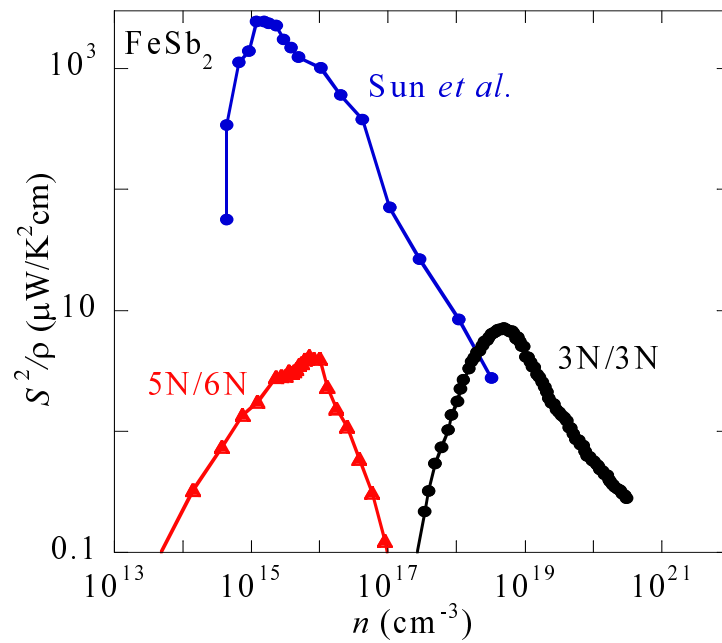


Figure 2.10: The carrier concentration dependence of the power factor on FeSb_2 . The 3N/3N sample plotted by the black solid circle shows the peak at around 10^{19} cm^{-3} , while the 5N/6N sample plotted by the red solid triangle has a peak at around 10^{16} cm^{-3} . Sun *et al.* reported a large power factor, which has a maximum value at almost the same position as that of 5N/6N.

Chapter 3

Magnetotransport properties

3.1 Introduction

In this chapter, we present magnetotransport properties of FeSb₂ single crystals (5N/6N) to investigate its electronic states at low temperatures. In the previous chapter, we found that the Seebeck coefficients are simply related to the carrier concentration: The large Seebeck coefficient is observed due to the extremely small carrier concentration. Moreover, this compound shows the peculiar temperature dependence of the mobility, which results in an unique carrier concentration dependence of the power factor. Although this compound is intrinsically the multi-band system, the carrier concentration and mobility were evaluated by the simple one-band model. Thus, to evaluate the carrier concentration and mobility more quantitatively, we study the magnetic field dependence of the magnetoresistance and Hall resistivity. Analyzing these properties, we discuss the electronic states of this compound.

3.2 Experiment

The electrical resistivity as a function of temperature was measured with the four terminal method in a magnetic field of 70 kOe from 100 down to 3 K, in which the magnetic field was applied perpendicular to current. Here, we eliminated the component of the Hall voltage V_H by measuring the voltage at +70 kOe and -70 kOe with the following equation; $V(70 \text{ kOe}) = [V(+70 \text{ kOe}) + V(-70 \text{ kOe})]/2$. The magnetic field dependence of the electrical and Hall resistivities was measured up to 70 kOe in the temperature range from 30 down to 3 K. These transport properties were measured in the Quantum Design Physical Properties Measurement System. For the magnetoresistance measurements, we employed the transverse configuration, i.e., with the current perpendicular to the magnetic field. We ob-

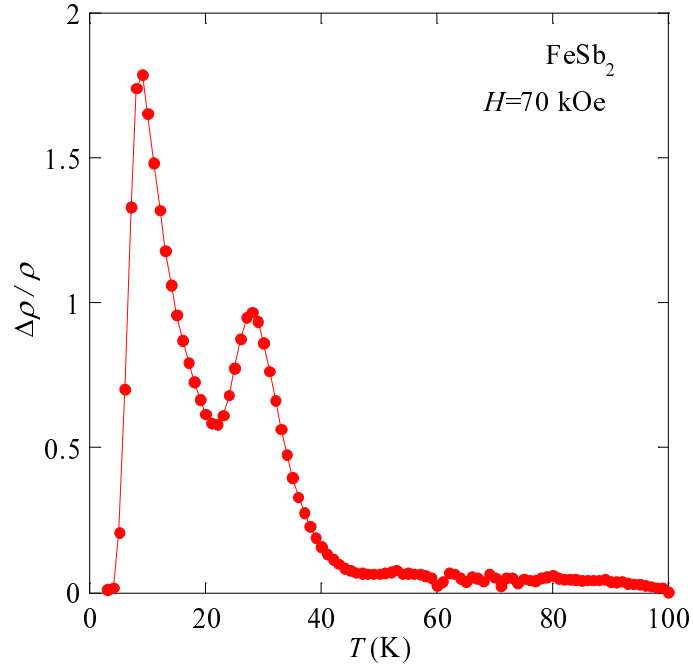


Figure 3.1: The temperature dependence of the magnetoresistance $\Delta\rho/\rho$ at $H = 70$ kOe below 100 K.

served no significant direction dependence with respect to the crystalline axes. For measurements of the Hall resistivity, the magnetic field was swept from +70 to -70 kOe, and the Hall voltage was determined as $V_H = \frac{1}{2}[V(+H) - V(-H)]$, where V is the voltage across the Hall terminals. All the measurements mentioned above were conducted to the 5N/6N sample.

3.3 Result and discussion

3.3.1 Temperature dependence of the magnetoresistance

The temperature dependence of the transverse magnetoresistance $\Delta\rho/\rho \equiv [\rho_{xx}(70 \text{ kOe}) - \rho_{xx}(0)]/\rho(0)$, where ρ_{xx} is the dc resistivity, is shown in Fig. 3.1. There are two peaks at 10 and 28 K, and the maximum value of the magnetoresistance reaches above 1.5 at 10 K, while the magneticresistance disappears below 4 K.

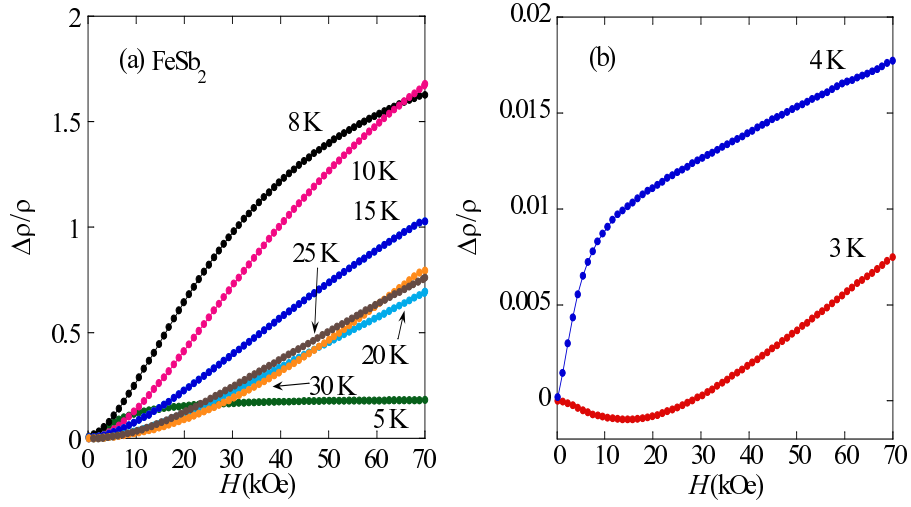


Figure 3.2: The transverse magnetoresistance $\Delta\rho/\rho$ from 30 to 3 K.

3.3.2 Magnetic field dependence of the magnetoresistance and the Hall resistivity

Figures 3.2(a) and 3.2(b) display the transverse magnetoresistance $\Delta\rho/\rho$, measured at various temperatures from 3 to 30 K. This compound shows an unusual field dependence of $\Delta\rho/\rho$ at all temperatures. From 30 down to 8 K, $\Delta\rho/\rho$ in low fields is proportional to H^2 similar to the conventional behavior, but in high fields, it increases almost linearly with increasing magnetic field above 15 K, and tends to saturate at 10 and 8 K. The large $\Delta\rho/\rho$ above 1.5 is observed in 70 kOe at 10 and 8 K, while below 5 K, $\Delta\rho/\rho$ is drastically suppressed. Moreover, at 3 K, a negative magnetoresistance is observed below 30 kOe.

An unusual behavior of the Hall resistivity ρ_{xy} is also observed at several temperatures, as shown in Figs. 3.3(a) and 3.3(b). The Hall resistivity is highly nonlinear in H at the moderately high magnetic fields, and from 4 to 8 K, the Hall resistivity has a peak at a certain magnetic field, whose position decreases with decreasing temperature.

3.3.3 Magnetic field dependence of the magnetoconductivity tensor

Magnetotransport properties are affected by the characteristic features of the physical quantities, such as the carrier concentration and mobility. We discuss the magnetic field dependence of the conductivity tensors to properly evaluate the

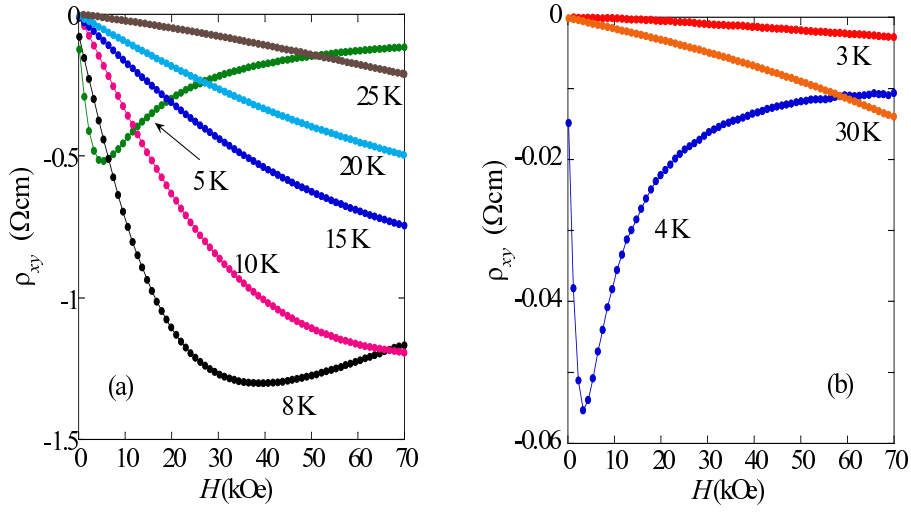


Figure 3.3: The Hall resistivity ρ_{xy} , as a function of the magnetic field measured at various temperatures from 30 to 3 K.

carrier concentration n and the mobility μ . We depict $\sigma_{xx} = \rho_{xx}/(\rho_{xx}^2 + \rho_{xy}^2)$ and $\sigma_{xy} = -\rho_{xy}/(\rho_{xx}^2 + \rho_{xy}^2)$ in the temperature range between 8 and 30 K in Figs. 3.4(a) and 3.4(b), respectively. The magnetic field dependence of σ_{xx} systematically changes with decreasing temperature: The absolute values are suppressed with decreasing temperature, maintaining these shapes. The values of σ_{xy} at 30 and 25 K saturate in high fields, and below 20 K, peaks are observed at a certain field and these positions systematically decrease with decreasing temperature. In Fig. 3.5, we show σ_{xx} and σ_{xy} below 5 K. These magnetic field dependences drastically change from 4 to 3 K. In the Boltzmann transport theory, the magnetic field dependence of the conductivity tensors is expressed by using n and μ (Appendix A. 1). Here, we analyze σ_{xx} and σ_{xy} with a two-carrier model, because the temperature dependences of S and R_H have a sign change at around 40 K, indicating the existence of at least two carriers. In this model, we assume that one carrier is of high mobility and the other is of low mobility ($\mu H \ll 1$), in which the H dependence of the conductivity tensors is described as

$$\sigma_{xx}(H) = n_{xx}e\mu_{xx}\frac{1}{1 + (\mu_{xx}H)^2} + C_{xx}, \quad (3.1)$$

$$\sigma_{xy}(H) = n_{xy}e\mu_{xy}^2H \left[\frac{1}{1 + (\mu_{xy}H)^2} + C_{xy} \right], \quad (3.2)$$

where n_{xx} (n_{xy}), μ_{xx} (μ_{xy}), and C_{xx} (C_{xy}) are the carrier concentrations, the carrier mobilities, and the low-mobility components for σ_{xx} (σ_{xy}), respectively. The

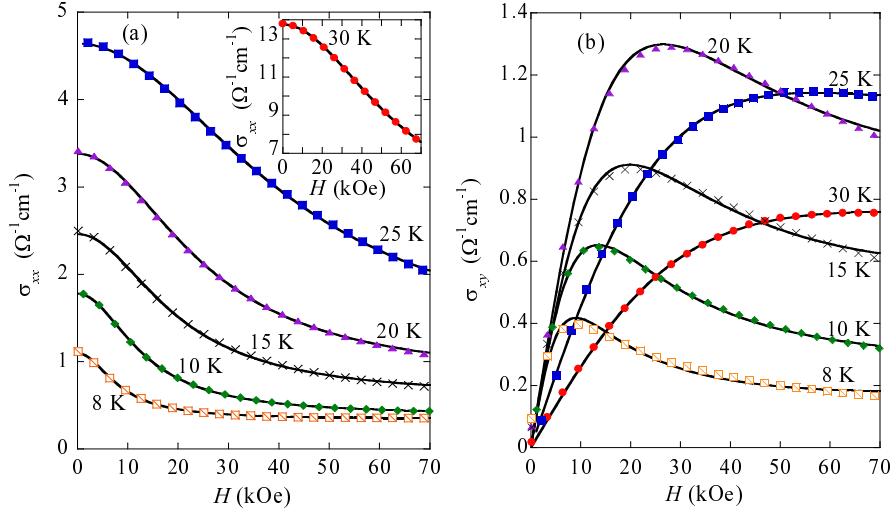


Figure 3.4: The magnetic field dependence of the conductivity tensor (a) σ_{xx} and (b) σ_{xy} from 8 to 30 K. Solid curves are the fitting calculation using Eqs. (3.1) and (3.2).

best fitting results of σ_{xx} and σ_{xy} with Eqs. (3.1) and (3.2) are drawn by solid curves in Figs. 3.4 and 3.5. However, the above two-carrier model cannot reproduce the data of σ_{xx} at 3 and 4 K and those of σ_{xy} at 3 K, and we will discuss this reason later.

3.3.4 Temperature dependence of the carrier concentration and mobility

From the fitting of the conductivity tensors, we evaluate the carrier concentration and carrier mobility. The carrier mobilities μ_{xx} and μ_{xy} are obtained independently from σ_{xx} and σ_{xy} . As shown in Fig. 3.6(a), the $1/T$ dependences of the carrier mobility μ_{xx} and μ_{xy} are in excellent agreement each other, justifying our evaluation for these quantities within the two-carrier model. n_{xx} and n_{xy} are also obtained independently, and show the same values each other, as shown in Fig. 3.6(b). In Fig. 3.6(c), the low mobility components C_{xx} and C_{xy} are presented. The mobilities μ_{low} estimated from C_{xx} and C_{xy} are less than 25 % of the high-mobility components at 10 K, and $\mu_{\text{low}}H \ll 1$ holds at low fields and even at high fields. Furthermore, we can consider that the fitting model using Eqs. (1) and (2) is still valid because the contribution of the low-mobility components to σ_{xx} and σ_{xy} is much smaller than that of high-mobility carriers.

Now we discuss the carrier mobility in this material. As shown in Fig. 3.6(a),

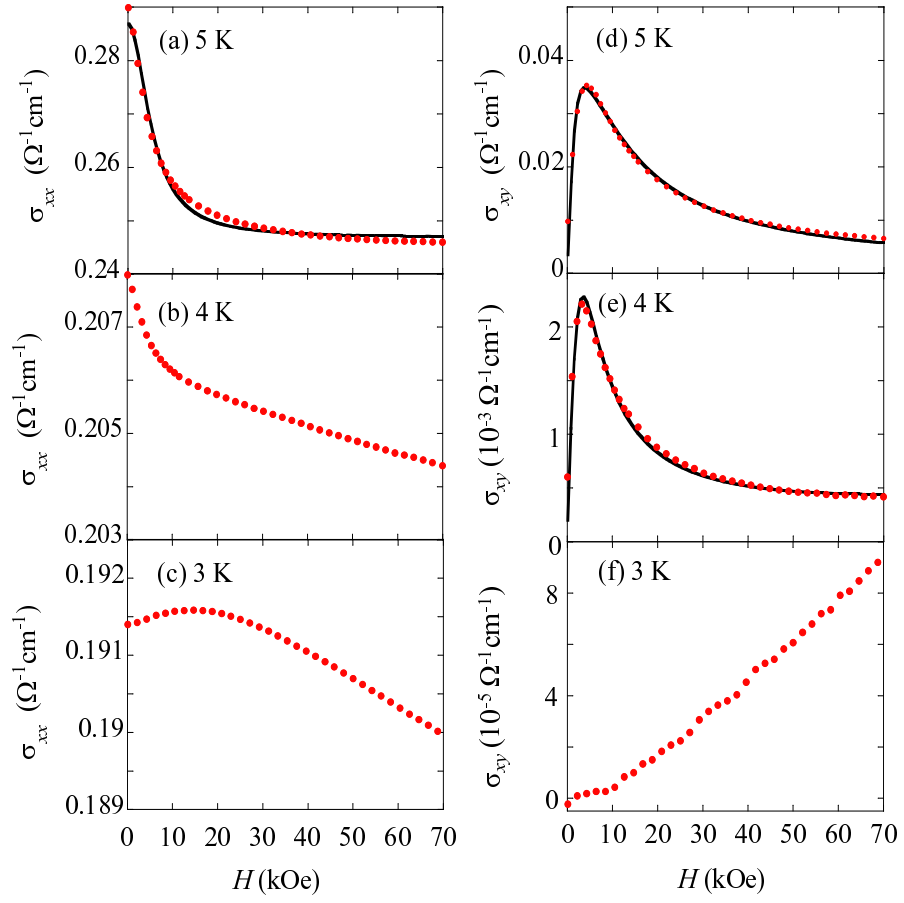


Figure 3.5: The magnetic field dependence of the conductivity tensor (a)-(c) σ_{xx} and (d)-(f) σ_{xy} from 3 to 5 K. Solid curves are the fitting calculation using Eqs. (3.1) and (3.2). σ_{xx} below 4 K and σ_{xy} at 3 K cannot be fitted with these equations.

the mobility of the dominant carrier dramatically increases from about $2000 \text{ cm}^2/\text{Vs}$ at 30 K to $\mu \simeq 28000 \text{ cm}^2/\text{Vs}$ at 4 K, which is a significantly large value, comparable to that of high-purity Si or Ge semiconductors.[42, 43] Such a large value of the mobility at low temperatures has been also observed in several Kondo insulators and charge-density-wave systems, because of an enhancement of the scattering time due to the gap opening.[37, 44] Previous studies of the transport properties have shown a large mobility in FeSb₂, which is obtained from the Hall coefficient R_H and the resistivity ρ ($\mu_H = |R_H|/\rho$).[18] This result is different from the present one: μ_H exhibits a broad peak around 8 K and its maximum value is five times smaller than ours, which is clearly due to the evaluation method. Hu *et al.* reported a giant carrier mobility of $\mu \simeq 8 \times 10^4 \text{ cm}^2/\text{Vs}$ near 10 K, which was estimated from the two carrier model, while they only use the magnetic field dependence of the Hall coefficient.[46] The nonlinearity of their raw data for $\rho_{xy}(H)$ at 10 K is, however, unclear compared with ours at the same temperature and this data can be plotted into our data between 30 and 25 K, which implies that μ is of the order of $10^3 \text{ cm}^2/\text{Vs}$. The fitting model in Ref. 28 can be used to the very-high-mobility compounds in which $\rho_{xy}(H)$ exhibits a strong nonlinear H dependence in a nonquantizing low-field range.[45] Thus, they might overestimate the carrier mobility in this system.

We next discuss the carrier concentration shown in Fig. 3.6(b). With decreasing temperature from 30 down to 4 K, it rapidly decreases from 10^{16} cm^{-3} (1 ppm/unit cell) to 10^{12} cm^{-3} (10^{-4} ppm/unit cell), which can be understood as thermally activation carriers. As shown by the dotted line, we evaluate the energy gap $\Delta = 6 \text{ meV}$ by the thermal activation function $n \propto \exp(-\Delta/2k_B T)$. The systematic study of the impurity effects on the transport properties shown in the previous chapter indicates that the electric conduction at low temperature is governed by the carrier concentration controlled by impurity in the Sb powder, which may suggest that the main carriers are excited from the impurity level located slightly below the bottom of the conduction band. In this picture, Δ corresponds to the energy gap between the impurity level and the bottom of the conduction band, implying that the gap Δ is unlikely to be a gap in the Kondo insulators.

3.3.5 Magnetotransport properties below 4 K

To examine the validity of the above picture, we focus on the magnetotransport properties below 4 K, where σ_{xx} failed in fitting with Eq. (3.1). As seen in Fig. 3.2(b), the magnitude of $\Delta\rho/\rho$ is extremely small compared to those above 5 K, and the negative magnetoresistance is observed around low magnetic fields at 3 K. The negative magnetoresistance has been widely observed in doped semiconductors in the low-temperature range because of a weak localization. [47, 48] In the case of As-doped Ge, carriers in the impurity band become dominant to the

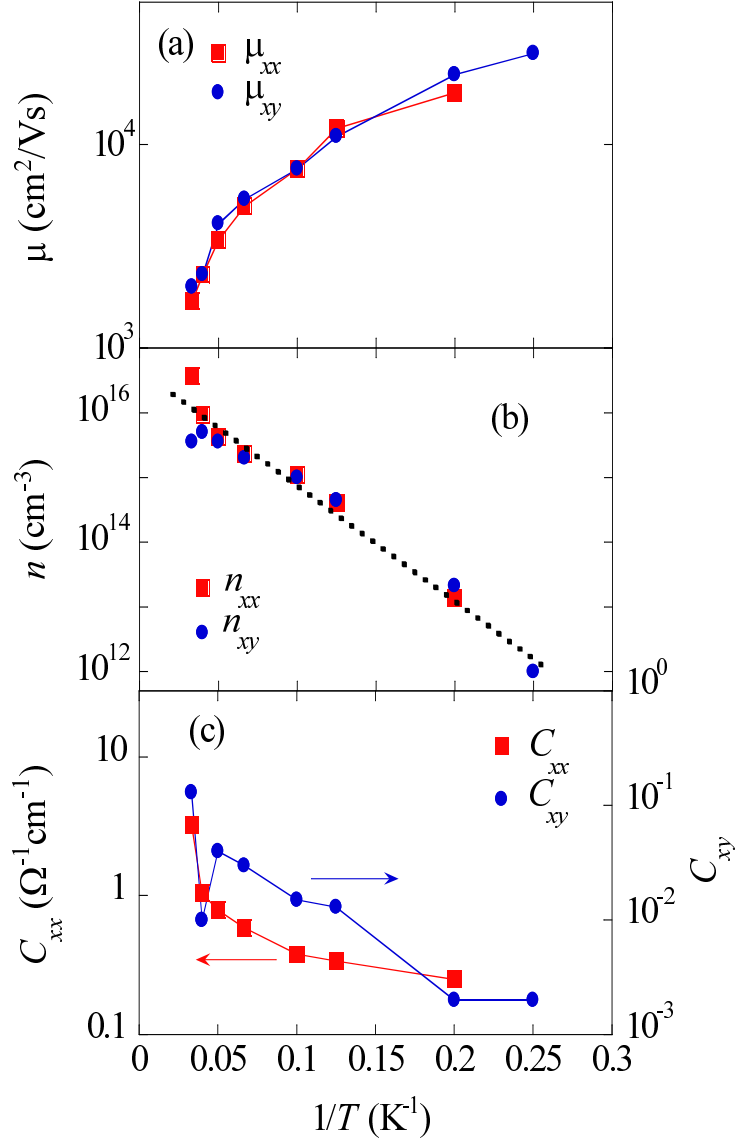


Figure 3.6: $1/T$ dependence of (a) the carrier mobility μ and (b) the carrier concentration n , and (c) the low-mobility components C_{xx} and C_{xy} , obtained from the fitting results for the conductivity tensors. The energy gap of $\Delta = 6$ meV is evaluated using the thermal activation function $n \propto \exp(-\Delta/2k_B T)$ shown as the dotted line in (b).

electric conduction at very low temperatures, where the thermal excitation carriers into the conduction band are negligibly small. Due to the random potential in the impurity band, the carriers are weakly localized, resulting in a negative magnetoresistance.[48] A striking similarity of the low-temperature magnetoresistive behavior between FeSb₂ and conventional semiconductors suggests a considerable impurity level in the electronic structure of FeSb₂: The impurity level exists slightly below (~ 6 meV) the bottom of the conduction band, and carriers in the impurity level are predominant on the electrical transport at 3 K.

3.4 Summary

We have measured the magnetic field dependence of the electrical and Hall resistivities of pure FeSb₂ single crystals and analyzed the conductivity tensors by using a two-carrier model to evaluate the carrier concentration and mobility. The mobility is significantly enhanced from 2000 cm²/Vs at 30 K to 28000 cm²/Vs at 4 K with decreasing temperature. The carrier concentration decreases from 1 down to 10⁻⁴ ppm/unit cell with decreasing temperature from 30 down to 4 K, from which we evaluate an energy gap of ~ 6 meV by the thermally activation function. Below 4 K, the magnetotransport behaviors drastically change and a negative magnetoresistance is observed at 3 K. Considering that the negative magnetoresistance due to a weak localization is often found in doped semiconductors, we think that there are considerable impurity levels in the electronic structure of FeSb₂. The magnetotransport studies reported in this chapter strongly suggests that the low-temperature transport properties of FeSb₂ are well understood as an extrinsic semiconductor with the ppm-level impurity.

Chapter 4

Pressure effect of transport properties to analyze the gap formation mechanism

4.1 Introduction

In this chapter, we show pressure effects of transport properties, and pressure dependence of the energy gap in FeSb₂. Previous studies have revealed that the large Seebeck coefficient and other transport properties are well understood as an extrinsic semiconductor with ppm-level impurities. However, some groups attribute the Seebeck coefficient to strong correlation effects, because some physical properties of FeSb₂ such as the magnetic susceptibility are similar to those of the Kondo insulators.[16, 17] Sun *et al.* proposed that the huge Seebeck coefficient is observed due to the unique band structure seen in Kondo insulators, in which the hybridization between the localized Fe 3*d*-orbitals and broad Sb 5*p* bands make a small energy gap and a steep variation of the density of states near the Fermi level.[18] Thus, we investigate whether the gap is formed by the Kondo interaction.

An important feature of the hybridization gap in the Kondo insulator is that the gap size is sensitive to the strength of the hybridization between the broad and narrow bands, which can be changed by compression/expansion of the lattice with physical pressure or chemical substitutions. In the 4*f*-electron Kondo insulator Ce₃Bi₄Pt₃, the application of physical pressure results in an increase in the gap size according to the expectation of the hybridization gap model.[51] In SmB₆ and YbB₁₂, the gap magnitude is also easily modified through the hybridization change by pressure, but in this case, pressure adversely affects to suppress the gap, which is possibly attributed to the ion-size difference between various 4*f*

configurations.[53, 54] Here, to clarify the origin of the gap formation mechanism in FeSb₂, we study the hydrostatic pressure effect on the energy gap through the electrical resistivity and magnetotransport measurements. Pressure changes the hybridization with remaining the imperfections of the crystal intact, from which we can discuss the band structure in this compound.

4.2 Experiment

The resistivity and the magnetotransport properties were measured in the pressure from 0 to 1.8 GPa for 5N/6N sample. The resistivity was measured from 300 down to 3 K, and the magnetic field dependence of the electrical and Hall resistivities was measured up to 70 kOe in the temperature range from 30 down to 5 K. These transport properties were measured with a conventional four-probe dc method using the Physical Property Measurement System (Quantum Design, Inc.) with a piston cylinder clamp cell made of BeCu (ElectroLAB Company) (Fig. 4.1). Samples were put on the sample stage by varnish as shown in Fig. 4.2. Daphne oil 7373 was used as a pressure-transmitting medium and the applied pressure was evaluated from the superconducting transition temperature of Pb placed near the sample (Fig. 4.3). The transition temperature of superconductivity decreases with increasing pressure at a rate of 0.348 K/GPa.[55]

4.3 Results and Discussion

4.3.1 Pressure effect of the electrical resistivity

Figure 4.4 shows the temperature dependence of the electrical resistivity ρ below 300 K at 0, 0.9 and 1.8 GPa. The insulating behavior is observed at 0 GPa, which can be separated two regions by a plateau near 20 K, indicating the existence of the two energy gaps in FeSb₂. [16, 25, 26, 18] Applying pressure, the magnitude of ρ increases both regions, and the plateau temperature increases from 20 to 30 K. We evaluate the large gap Δ_1 at each pressure using the data above 100 K, fitted with the thermal activation function of $\rho = \rho_0 \exp(\Delta_1/2k_B T)$, as shown by the dotted line in Fig. 4.4(b). Apparently, the slope increases with pressure, showing that the energy gap is enhanced from 30 to 40 meV. This enhancement is consistent with that for the polycrystalline sample reported by Mani *et al.*[59] In contrast, we cannot precisely evaluate the pressure dependence of the small gap Δ_2 , since the carrier mobility is strongly enhanced with decreasing temperature below 30 K, leading to the overestimation of the charge gap obtained from the resistivity.

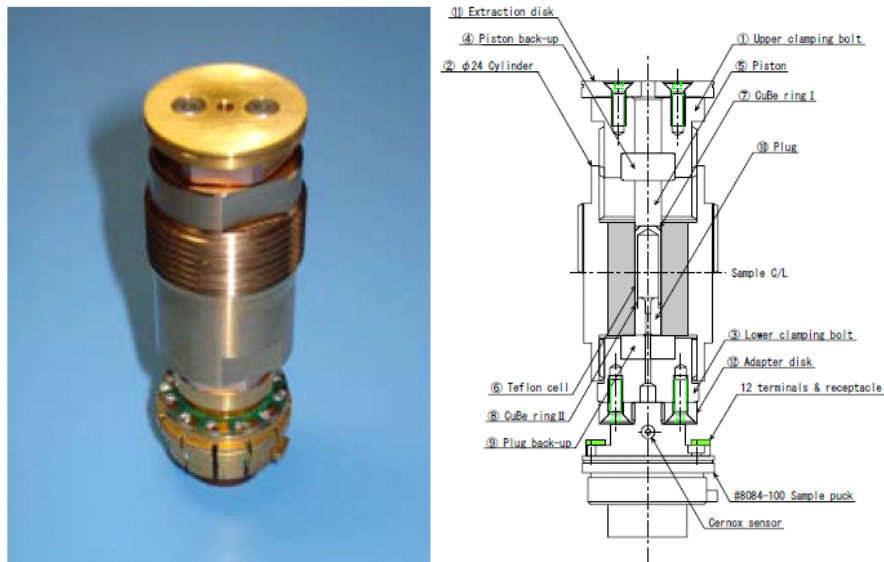


Figure 4.1: A picture and schematic diagram of a piston cylinder clamp cell made of BeCu (ElectroLAB Company).

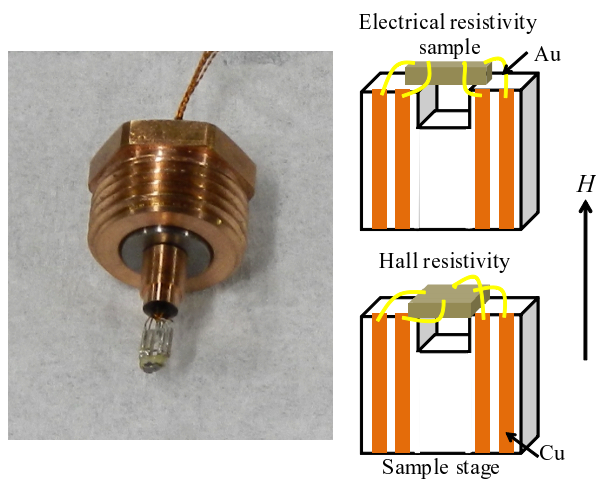


Figure 4.2: A picture and schematic figures of the sample stage of pressure measurements. The diameter of sample space is about 4 mm.

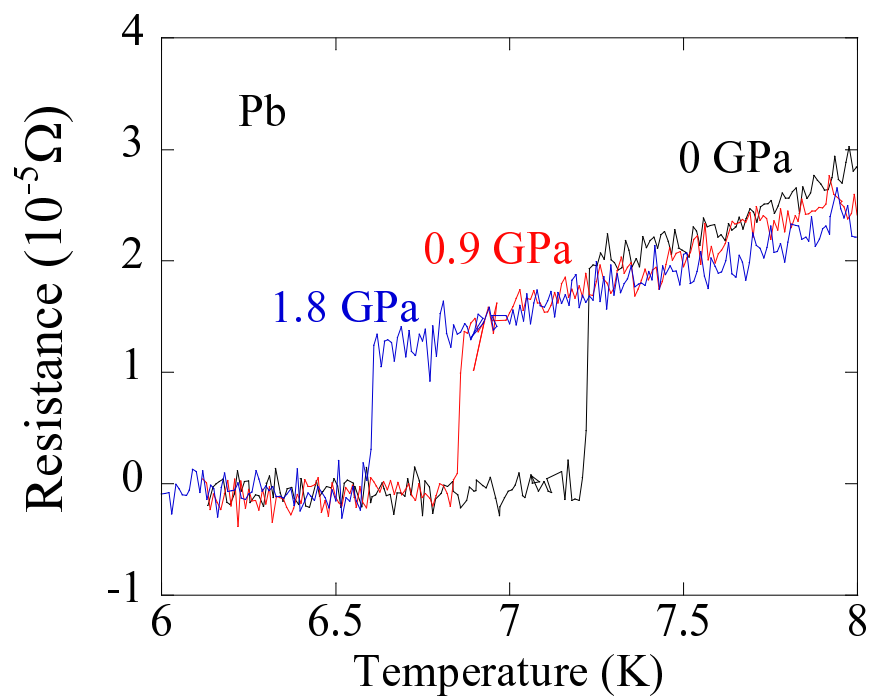


Figure 4.3: The temperature dependence of the resistivity of Pb under several pressures. The transition temperature of superconductivity decreases with increasing pressure.

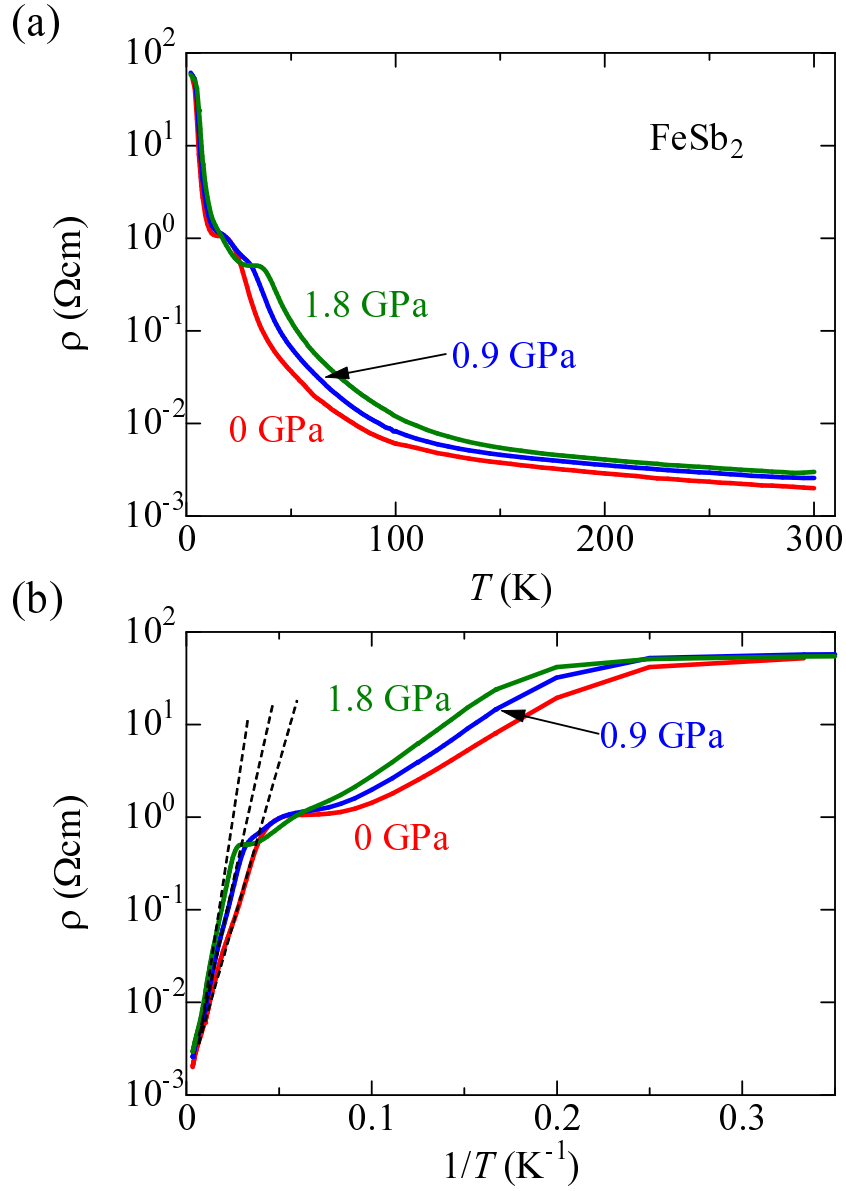


Figure 4.4: (a) The temperature dependence of the resistivity ρ at various pressures. (b) The resistivity as a function of $1/T$, where large energy gaps are evaluated by an activation function $\rho \propto \exp(\Delta_1/2k_B T)$, plotted as dotted lines.

4.3.2 Pressure dependence of the magnetotransport properties

In Figs. 4.5(a)-(f), we show the magnetic field dependence of the Hall resistivity ρ_{xy} and the transverse magnetoresistance $\Delta\rho/\rho_0 \equiv [\rho_{xx}(H) - \rho_{xx}(0)]/\rho_{xx}(0)$, measured at various temperatures from 5 to 30 K at 0, 0.9 and 1.8 GPa. We used a different sample of 5N/6N and we find that the field dependence of ρ_{xy} and $\Delta\rho/\rho_0$ is essentially the same at ambient pressure as was shown in Chapter 3. ρ_{xy} and $\Delta\rho/\rho_0$ at high pressure are qualitatively similar to those at ambient pressure, while quantitative values are changed with pressure, indicating the change of the physical quantities.

To see the pressure dependence of the carrier concentration $n(T)$ and $\mu(T)$, we analyze the conductivity tensor $\sigma_{xy} = -\rho_{xy}/(\rho_{xx}^2 + \rho_{xy}^2)$ using the same method as shown in Chapter 3. The unique field dependence of σ_{xy} , is obtained at various pressures, as shown in Figs. 4.6(a)-(f). We fit these data with Eq. (3.2), and the best agreements of σ_{xy} are shown by the solid curves in Fig. 4.6. The mobility estimated from C_{xy} is about 15 % of the high-mobility component at all temperatures, and therefore, $\mu_{\text{low}}H \ll 1$ holds, and our model is valid for all conditions.

4.3.3 Analysis of the pressure dependence of the carrier concentration and the mobility

Here, we display the temperature dependence of the carrier concentration and mobility in Figs. 4.7(a) and 4.7(b) obtained from the above fitting. The mobilities increase with decreasing temperature as observed previously and are not affected well by pressure. The carrier concentrations show a semiconducting-like temperature dependence. To evaluate the small energy gap Δ_2 , we use an activation function of $n = n_0 \exp(-\Delta_2/2k_B T)$, described as the dotted lines in Fig. 4.7(b). The extrapolated lines using the data below 10 K deviate from the data above 20 K, because $\Delta_2/2k_B$ is of the order of 10 K. Above 10 K, the thermal fluctuation becomes comparable to the gap energy, and hence n does not follow the activation function. From the fitting, we evaluate the pressure dependence of the energy gap Δ_2 , which increases from 12 to 15 meV at 1.8 GPa. We depict the pressure dependence of both Δ_1 and Δ_2 in Fig. 4.8, showing that the enhancement of the energy gap Δ_1 is larger than that of Δ_2 .

4.3.4 Origin of the gap enhancement of Δ_1

Here, we attempt to understand an origin of the pressure dependence of Δ_1 . The gap enhancement is expected from a band calculation by Wu *et al.*: The gap of 0.2 eV at ambient pressure increases to 0.25 eV at 5 GPa.[56] Conventional semiconductors show the gap enhancements of order of 10 meV/GPa, since the periodic

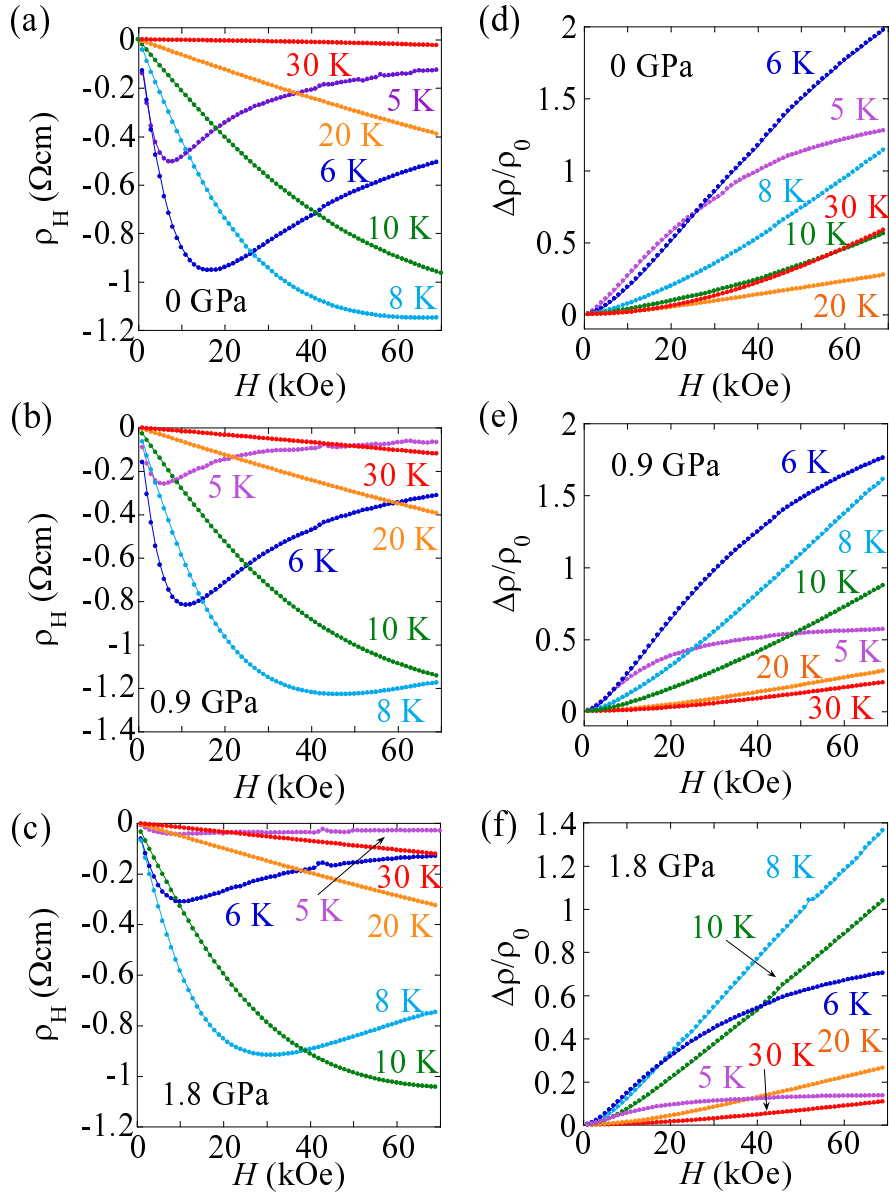


Figure 4.5: (a)-(c) The Hall resistivity ρ_{xy} , and (d)-(f) the transverse magnetoresistance $\Delta\rho/\rho$ as a function of the magnetic field measured at various pressures.

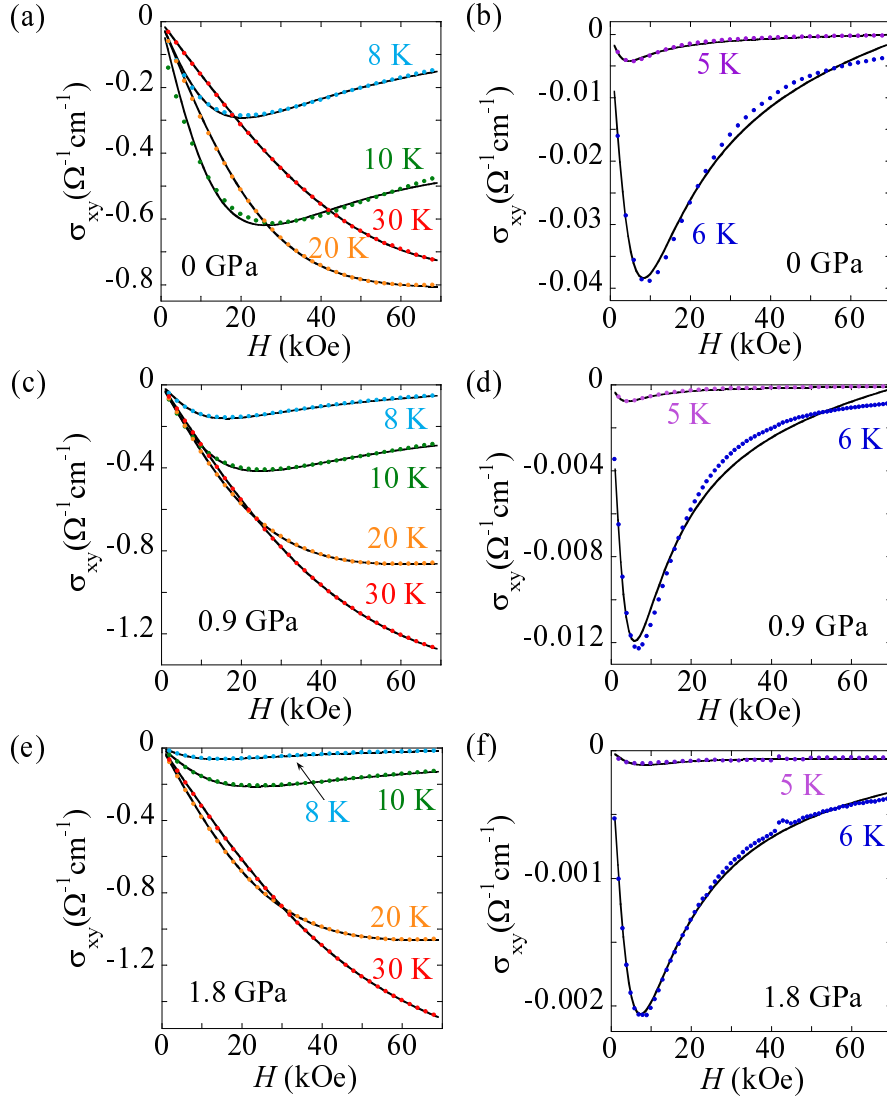


Figure 4.6: (a)-(f) The magnetic field dependence of the conductivity tensor σ_{xy} at various pressures from 5 to 30 K. Solid curves are the fitting curves using Eq. (3.2).

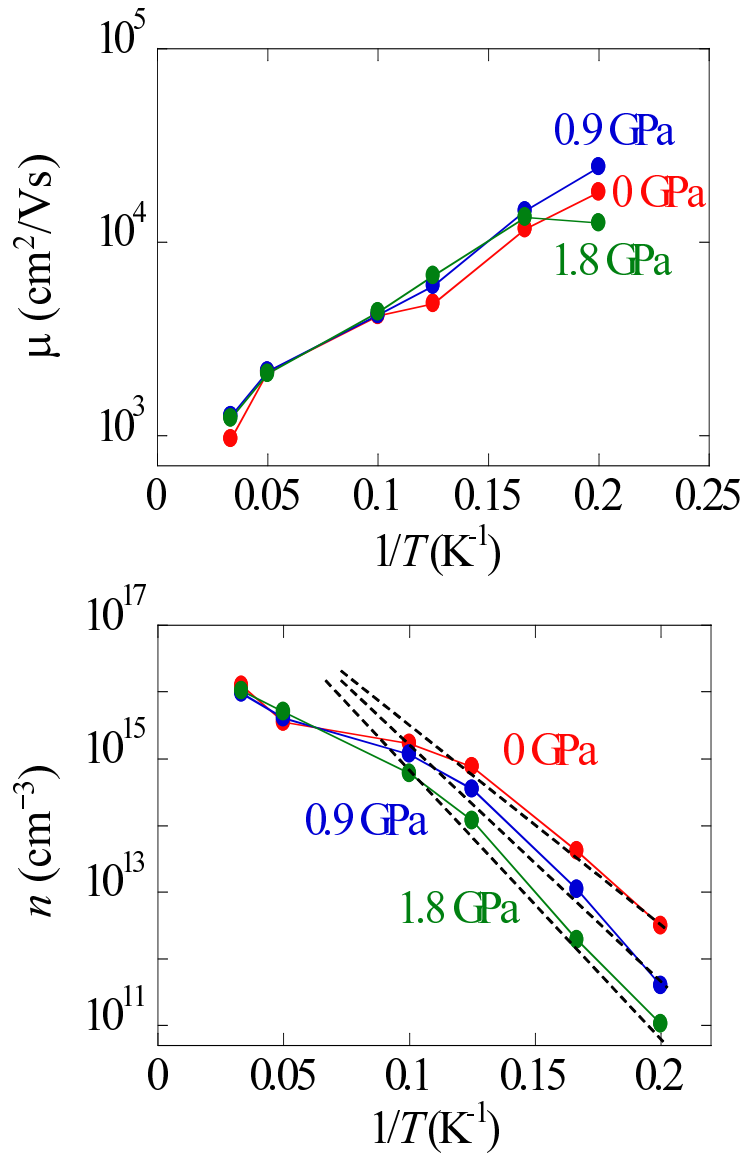


Figure 4.7: $1/T$ dependence of (a) the carrier mobility μ and (b) the carrier concentration n , obtained from the fitting results for σ_{xy} . The dotted lines are the fitting results to evaluate the small energy gap by the thermal activation function $n \propto \exp(-\Delta_2/2k_B T)$.

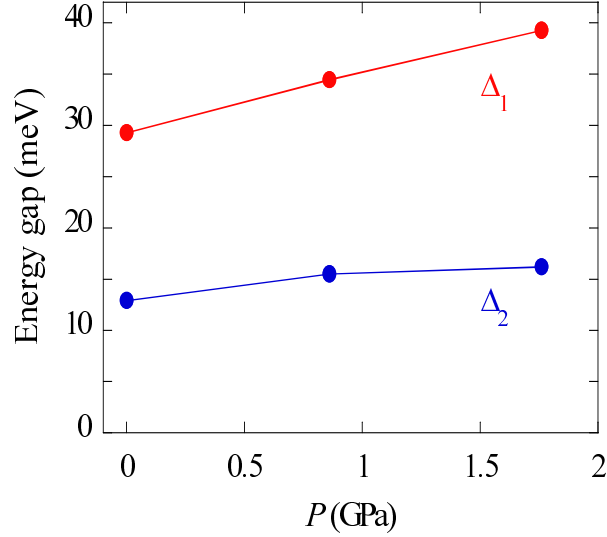


Figure 4.8: The pressure dependence of energy gaps of Δ_1 (red circle) and Δ_2 (blue circle).

potential of electron in these material can vary by the lattice compression/expansion.[57, 58] These relative changes of the energy gaps are almost the same as that of our sample, suggesting that the enhancement of Δ_1 can be explained by a simple band model. On the other hand, this enhancement can be accounted for a hybridization between the narrow d -bands and the broad conduction bands due to the Kondo mechanism. In the Kondo system, the gap size is modified by changing the strength of the hybridization V . Applying pressure, V tends to increase by approaching the narrow d/f band to the conduction band, leading to increase the energy gap (Appendix A. 2).[59, 60, 61] The relative change of the gap size enhancement of Δ_1 is almost the same as that of FeSi, which is considered as a d -electron Kondo insulator.[33] The relation between the strongly correlated effect and the gap formation mechanism of FeSb₂ was suggested by an optical measurement, which observed an unusual behavior that an opening of the gap is associated with a large transfer of the spectral weight over an energy range of ~ 1 eV compared with the value of the energy gap.[62] From the above results, the pressure effect cannot directly clarify that Δ_1 is formed by the simple band model or an electron correlation effect such as the Kondo mechanism.

4.3.5 Origin of the gap enhancement of Δ_2 : Association with the Kondo mechanism.

An origin of the small gap Δ_2 is important because some groups think that the huge Seebeck coefficient is observed due to the small energy gap of Δ_2 opened by strong correlation effects.[16, 25, 26, 18] The energy gap increases from 12 meV at 0 GPa to 15 meV at 1.8 GPa, and the enhancement is less than half compared with that for Δ_1 . In Kondo systems, the gap will be quite sensitive to the high pressure compared with the gap of the single particle band structure. Actually, a typical f -electron Kondo insulator $\text{Ce}_3\text{Bi}_4\text{Pt}_3$, which has a Kondo gap of 50 K at ambient pressure, [51] shows more sensitive pressure dependence of the energy gap. This Kondo gap increases nearly linearly with pressure, and becomes twice at 10 kbar. The small pressure effect of Δ_2 seems to indicate that Δ_2 does not come from the Kondo effect. This result is consistent with the previous studies, where we suggested that Δ_2 is a gap between the impurity band and the conduction band. The magnitude of the carrier concentration $n = n_0 \exp(-\Delta_2/2k_B T)$ also indicates that the gap Δ_2 is unlikely to come from the Kondo gap. As shown in Fig. 4.7(b), n_0 falls on $10^{18} - 10^{19} \text{ cm}^{-3}$, which corresponds to 0.01 carrier per unit cell. The value of n_0 roughly indicates a saturated carrier concentration at high temperature, and accordingly the small n_0 implies that very few carriers are available. In Kondo insulators, n_0 corresponds to the density of states of the conduction band, being $10^2 - 10^3$ times larger.[52]

Considering the above analysis, we depict a schematic band picture of FeSb_2 in Fig. 4.9, showing that Δ_1 is a gap between the conduction band and the valence band, and the impurity band exists in the band gap, and Δ_2 is a gap from the impurity band to the conduction band. In this case, Δ_2 increases with increasing Δ_1 . This model can qualitatively explain the smaller pressure dependence of Δ_2 , inferring that Δ_2 is not directly related to the Kondo gap.

4.3.6 Origin of the huge Seebeck coefficient

Finally, we discuss the origin of the huge Seebeck coefficient S . The Seebeck coefficient is calculated using a nondegenerate model expressed as [23]

$$S = \pm \frac{k_B}{e} \left(\frac{\Delta}{k_B T} + r + \frac{5}{2} \right), \quad (4.1)$$

where r is a scattering parameter. Now we calculate the value of S using $\Delta = 12$ meV evaluated from the $1/T$ dependence of the carrier concentration, and obtain $|S| \sim 700 \mu\text{V/K}$ at 20 K. Here, we assume $r = 3/2$, which is used in conventional semiconductors. The calculated value is close to, but nearly two times smaller than the experimental results of $S = -1500 \mu\text{V/K}$. An electron-electron

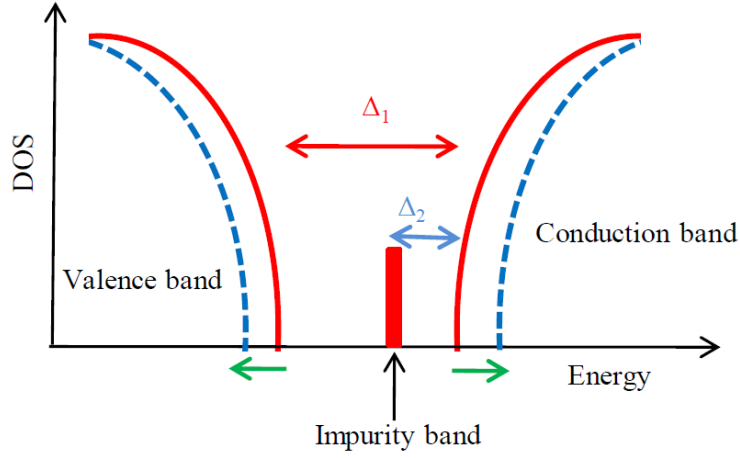


Figure 4.9: The schematic band picture of FeSb₂. The impurity band exists between the conduction and valence bands. Δ_1 is enhanced because the conduction and valence band energy shift due to the change of the hybridization strength between the narrow d bands and broad p bands. Δ_2 also increases with the energy shift of the conduction band.

correlation is unlikely to be the origin of this deviation because it has an insignificant effect on the Seebeck coefficient in an insulating regime as reported in Ref. 35, in which the Seebeck coefficient is calculated with the Kubo formula using the band calculation.

The phonon-drag effect plays an essential role for an enhancement of the Seebeck coefficient at the low-temperature in many pure semiconductors.[39, 40, 41] The phonon-drag term in the Seebeck coefficient can be approximately expressed as $S_p = \beta v_p l_p / \mu T$, where v_p and l_p are the velocity and the mean free path of a phonon, respectively, and $0 < \beta < 1$ is a parameter which characterizes the relative strength of the electron-phonon interaction.[41, 49] Some groups observed the temperature dependence of the thermal conductivity, which has a large value below 30 K, as shown in Fig. 4.10(a). From this result, a long mean free path of $l_p \simeq 10 \mu\text{m}$ at 20 K was estimated.[16, 25, 26] In addition, Bienten *et al.* calculated the sound velocity to be 3000 m/s with a Debye model with $\theta_D = 340$ K.[16] Using these parameters, S_p at 20 K is estimated to be nearly 3 mV/K at the maximum, which suggests that the phonon-drag effect can yield a measurable contribution to the Seebeck coefficient in our compounds. On the other hand, the phonon-drag effect in heavily doped semiconductors becomes negligibly small because the mean free path of the phonon is strongly affected by the high impurity and electron concentration.[41] For example, the Seebeck coefficient of Si

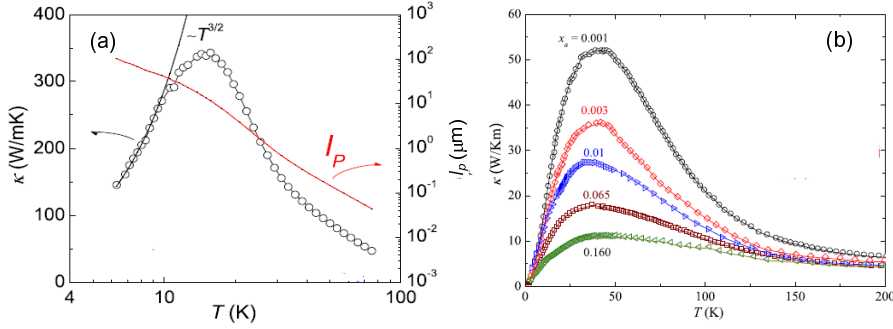


Figure 4.10: (a) The temperature dependence of a thermal conductivity κ and a phonon mean free path l_p . l_p was evaluated from the formula $\kappa_L = 1/2C_L v_s l_p$, where κ_L is the lattice contribution to the thermal conductivity estimated from the Wiedemann-Franz law, C_L is a lattice contribution to specific heat, and v_s is the sound velocity of 3116 ms^{-1} . [16, 26] (b) The thermal conductivity of $\text{FeSb}_{2-x}\text{Te}_x$, which is strongly suppressed by Te doping. [50]

shows a strong impurity effect: A single crystal doped with P atoms of $2.8 \times 10^{16} \text{ cm}^{-3}$ shows a huge Seebeck coefficient of 10 meV at 30 K due to the phonon-drag effect, while a single crystal doped with As atoms of $1.7 \times 10^{19} \text{ cm}^{-3}$ has a much smaller value of $400 \mu\text{V/K}$ at 300 K and this value decreases with decreasing temperature, explained by the conventional degenerate model (Eq. (2.2)). Actually, the thermal conductivity of Te-doped $\text{FeSb}_{2-x}\text{Te}_x$ with $x = 0$ is suppressed about one order of magnitude with $x = 0.001$ (Fig. 4.10), the impurity concentration of which is compatible with the 3N/3N sample, and then the Seebeck coefficient of this sample becomes small and can be only explained by the diffusion part discussed in Chapter 2. [50]

4.4 Summary

We have measured the temperature and magnetic field dependences of the electrical and Hall resistivity of high-quality FeSb_2 single crystals at various pressures, and analyzed the pressure dependence of the large and small energy gaps. The large energy gap Δ_1 increases from 30 to 40 meV in going from 0 to 1.8 GPa, which implies that the hybridization between the narrow d bands and the broad p bands is important for Δ_1 to some extent. On the other hand, a weak pressure dependence of the small gap Δ_2 is observed. This weak pressure dependence suggests that the origin of the gap is not associated with strongly correlated effects such as the Kondo effect, because a typical $4f$ -Kondo insulator $\text{Ce}_3\text{Bi}_4\text{Pt}_3$ shows

a sensitive pressure effect that the relative enhancement of the gap is 5 times larger than that of our sample. We propose a band picture that Δ_2 is a gap between an impurity level and a conduction band, which naturally explains the temperature and pressure dependences of the transport properties. As the origin of the huge Seebeck coefficient, the phonon-drag effect may work, but the electron correlation effect is secondary.

Chapter 5

Conclusion

The narrow gap semiconductor FeSb_2 has been extensively studied because of an anomalously large Seebeck coefficient at low temperature (~ -45 mV/K at 10 K). This large value cannot be explained by the conventional theories and the effect of the electron-electron correlation such as the Kondo mechanism is proposed to understand this intriguing feature. In the present study, to clarify the origin of the huge Seebeck coefficient, we have conducted three experiments.

First, we investigated the systematic impurity effect on the magnetic and transport properties in the singly crystal of FeSb_2 . In this study, we grew the single crystals with metal powders of different purities and showed that the purity of Sb powders strongly affects the physical properties. In particular, the large absolute value of the Seebeck coefficient (~ 1500 $\mu\text{V/K}$) was observed in single crystals with the Sb 6N powder, while a small value of 500 $\mu\text{V/K}$ was observed in single crystals with the Sb 3N powder. These different values can be understood as the conduction carriers are supplied by Sb impurities, and then the large difference of the carrier concentration is realized in this compound. In the purer single crystal, the carrier concentration is less than 10^{16} cm^{-3} below 30 K, indicating that this compound is a semiconductor with the extremely small carrier concentration.

Next, to investigate an electronic structure of FeSb_2 , we measured magnetotransport properties below 30 K, in which the large Seebeck coefficient was observed. The magnetoresistance and Hall resistivity show the peculiar magnetic field dependence, suggesting the characteristic features of physical quantities such as the carrier concentration and the mobility. We analyzed the magnetic field dependence of conductivity tensors with the experimental data using the two-carrier model, and evaluated more precise values of the carrier concentration and the mobility. We find that this compound is a semiconductor with a high mobility ~ 20000 cm^2/Vs at 4 K and a small carrier concentration less than 10^{16} cm^{-3} , which are consistent with conclusion in the impurity effect. Moreover, a negative magnetoresistance at weak fields is observed at 3 K, indicating that the energy gap

is formed between the conduction band and impurity band. However, from the analogy to the physical properties of Kondo insulators, the gap origin is still in controversial because some groups proposed that the small gap is formed by the strong electron correlation.

Finally, to investigate the gap formation mechanism, we studied a pressure dependence of the energy gap, because the gap size is very sensitive to pressure in the Kondo insulators. In this study, we evaluated the gap size with the electrical resistivity and the Hall resistivity from 0 to 1.8 GPa. FeSb₂ has two energy gaps of $\Delta_1 \sim 30$ meV and $\Delta_2 \sim 10$ meV at 0 GPa. A substantial enhancement of the energy gap was observed in Δ_1 , suggesting that the energy gap is formed due to the hybridization between Fe *d*-orbitals and Sb *p*-orbitals. In contrast, Δ_2 shows a weak pressure dependence compared with typical Kondo insulators, such as Ce₃Bi₄Pt₃. To explain the above pressure effect of the energy gaps, we propose a reasonable band picture that Δ_2 is the gap between the conduction and impurity band instead of the Kondo gap. Thus, we think that the strong correlation effect such as the Kondo mechanism is not relevant to be the origin of the huge Seebeck coefficient, and propose the phonon-drag effect as this origin, which is usually observed in very pure semiconductors.

Appendix

A.1 Conductivity tensor

We describe the magnetic field dependence of the conduction tensors. Here, we think the motion of electrons with a classical theory. An equation of motion for an electron in the magnetic field can be written by

$$m d\mathbf{v}/dt = -e(\mathbf{E} + \mathbf{v} \times \mathbf{B}) - \frac{1}{\tau} m \mathbf{v}, \quad (5.1)$$

where, \mathbf{E} and \mathbf{B} are the electric field and the magnetic field, respectively. In this equation, we introduce $-\frac{1}{\tau} m \mathbf{v}$ as a phenomenological friction term. When the magnetic field is directed to z -axis ($\mathbf{B} = (0, 0, B)$), the above equation is described as

$$\dot{v}_x = -\frac{e}{m}(E_x + v_y B) - \frac{1}{\tau} v_x, \quad (5.2)$$

$$\dot{v}_y = -\frac{e}{m}(E_y - v_x B) - \frac{1}{\tau} v_y, \quad (5.3)$$

$$\dot{v}_z = -\frac{e}{m} E_z - \frac{1}{\tau} v_z. \quad (5.4)$$

In the steady state of $d\mathbf{v}/dt = 0$, above equations are expressed by

$$0 = -\frac{e}{m} E_x + \omega_c v_y - \frac{1}{\tau} v_x, \quad (5.5)$$

$$0 = -\frac{e}{m} E_y + \omega_c v_x - \frac{1}{\tau} v_y, \quad (5.6)$$

$$0 = -\frac{e}{m} E_z - \frac{1}{\tau} v_z, \quad (5.7)$$

where $\omega_c \equiv \frac{eB}{m}$, which is the cyclotron angular frequency. With these equations, we get $\mathbf{J} = -ne\mathbf{v}$ as

$$J_x = \frac{ne^2\tau}{m} \frac{(E_x - \omega_c\tau E_y)}{1 + (\omega_c\tau)^2}, \quad (5.8)$$

$$J_y = \frac{ne^2\tau}{m} \frac{(E_y + \omega_c\tau E_x)}{1 + (\omega_c\tau)^2}, \quad (5.9)$$

$$J_x = \frac{ne^2\tau}{m} E_z. \quad (5.10)$$

We can change these equations to a matrix expression as

$$\begin{pmatrix} J_x \\ J_y \\ J_z \end{pmatrix} = \frac{ne^2\tau}{m} \begin{pmatrix} \frac{1}{1+(\omega_c\tau)^2} & \frac{-\omega_c\tau}{1+(\omega_c\tau)^2} & 0 \\ \frac{\omega_c\tau}{1+(\omega_c\tau)^2} & \frac{1}{1+(\omega_c\tau)^2} & 0 \\ 0 & 0 & 1 \end{pmatrix} \begin{pmatrix} E_x \\ E_y \\ E_z \end{pmatrix} \quad (5.11)$$

Thus, defining the conductivity tensor $\tilde{\sigma}$ as $\mathbf{J} = \tilde{\sigma}\mathbf{E}$, each component of conductivity tensors can be described as

$$\sigma_{xx} = \sigma_{yy} = \frac{1}{1 + (\omega_c\tau)^2} \sigma_0, \quad (5.12)$$

$$-\sigma_{xy} = \sigma_{yx} = \frac{\omega_c\tau}{1 + (\omega_c\tau)^2} \sigma_0, \quad (5.13)$$

$$\sigma_{zz} = \sigma_0, \quad (5.14)$$

where $\sigma_0 = \frac{ne^2\tau}{m}$.

A.2 Gap of Kondo insulator

To describe the Kondo system, we usually use a periodic Anderson model (PAM);

$$H = \sum_{\mathbf{k}\sigma} \epsilon_{\mathbf{k}} C_{\mathbf{k}\sigma}^+ C_{\mathbf{k}\sigma} + E_f \sum_{i\sigma} n_{f_i\sigma} + U \sum_i n_{f_i\uparrow} n_{f_i\downarrow} + \sum_{i\mathbf{k}\sigma} i\mathbf{k}\sigma (V_{\mathbf{k}} e^{i\mathbf{k}\mathbf{R}_i} f_{i\sigma}^+ C_{\mathbf{k}\sigma} + H.c.), \quad (5.15)$$

where $\epsilon_{\mathbf{k}}$ is energy of conduction electrons (s - or p - orbital electrons), E_f is energy of f -orbital electrons, $V_{\mathbf{k}}$ is the overlap integral between the conduction and f -orbital electrons. $C_{\mathbf{k}\sigma}$ ($C_{\mathbf{k}\sigma}^+$), and $f_{i\sigma}$ ($f_{i\sigma}^+$) are creation (annihilation) operators of conduction electrons with a wave number \mathbf{k} and a spin σ , and the f -orbital electrons on the i site with a spin σ , respectively, and $n_{f_i\uparrow\text{or}\downarrow}$ is the carrier number operator of f -orbital electrons. When U (Coulomb interaction between f electrons) is zero, the eigenenergy can be calculated as

$$E_k^{(\pm)} = \frac{\epsilon_k + E_f}{2} \pm \sqrt{\left(\frac{\epsilon_k - E_f}{2}\right)^2 + V_{\mathbf{k}}^2}, \quad (5.16)$$

where we use the Fourier transform of $f_{\mathbf{k}} = N^{-1/2} \sum_i f_i e^{-i\mathbf{k}\cdot\mathbf{R}_i}$. Assuming $V_{\mathbf{k}} = V = \text{constant}$, the indirect energy gap E_g^{ind} and the direct energy gap E_g^{dir} of the Kondo insulator can be written as

$$\begin{aligned}
E_g^{ind} &= E_{\mathbf{k}}^{(+)}(\epsilon_{\mathbf{k}} = -W) - E_{\mathbf{k}}^{(-)}(\epsilon_{\mathbf{k}} = +W) \\
&= \left(\frac{-W}{2} + \sqrt{\frac{W^2}{4} + V^2} \right) - \left(\frac{W}{2} - \sqrt{\frac{W^2}{4} + V^2} \right) \\
&= -W + \sqrt{W^2 + 4V^2} \\
&\rightarrow \frac{2V^2}{W} (V \ll W),
\end{aligned} \tag{5.17}$$

and

$$E_g^{dir} = E_{\mathbf{k}}^{(+)}(\epsilon_{\mathbf{k}} = E_f) - E_{\mathbf{k}}^{(-)}(\epsilon_{\mathbf{k}} = E_f) = 2V, \tag{5.18}$$

respectively. Here, $2W$ is the band width of the conduction band. These brief calculations indicate that the energy gap of the Kondo insulator increases with increasing V .

References

- [1] T. J. Seebeck, *Abh. Preuss. Akad. Wiss.* p. 265 (1822-1823).
- [2] A. F. Ioffe, *Semiconductor Thermoelements and Thermoelectric Cooling* Infosearch Ltd., London (1957).
- [3] P. H. Egli, ed., *Thermoelectricity* Wiley, New York (1961).
- [4] C. A. Domenicali, *J. Appl. Phys.* **25**, 1310 (1954).
- [5] P. J. Price, *Philos. Mag.* **46**, 1252 (1955).
- [6] P. J. Price, *Phys. Rev.* **104**, 1223 (1956).
- [7] R. P. Chasmar, and R. Stratton, *J. Electron. Control* **7**, 52 (1959).
- [8] L. D. Hicks and M. S. Dresselhaus, *Phys. Rev. B* **47**, 12727 (1993).
- [9] G. A. Slack, *CRC Handbook of Thermoelectrics* CRC press UK, Edited by D. M. Rowe p. 407 (1995).
- [10] J. W. Sharp, E. C. Jones, R. K. Williams, P. M. Martin, and B. C. Sales, *J. Appl. Phys.* **78**, 1013 (1995).
- [11] G. S. Nolas, T. J. R. Weakly, J. L. Chon, R. Sharm, *Phys. Rev. B* **61**, 3845 (2000).
- [12] J. G. Bednorz, and K. A. Z. Muller, *Phys. B* **64**, 189 (1986).
- [13] I. Terasaki, Y. Sasago, and K. Uchinokura, *Phys. Rev. B* **56** R12685 (1997).
- [14] C. D. W. Jones, K. A. Regan, and F. J. DiSalvo, *Phys. Rev. B* **58**, 16057 (1998).
- [15] G. D. Mahan, *Solid State Phys.* **51**, 81 (1998).
- [16] A. Bentien, S. Johnsen, G. K. H. Madsen, B. B. Iversen, and F. Steglich, *Europhys. Lett.* **80**, 17008 (2007).

- [17] A. Bentien, G. K. H. Madsen, S. Johnsen, and B. B. Iversen, *Phys. Rev. B* **74**, 205105 (2006).
- [18] P. Sun, N. Oeschler, S. Johnsen, B. B. Iversen, and F. Steglich, *Dalton Trans.* **39**, 1012 (2010).
- [19] N. W. Ashcroft, and N. D. Mermin, *Solid State Physics* Saunders College Publishing, (1988).
- [20] J. M. Ziman, *Principles of the Theory of Solids* Cambridge University Press, (1972).
- [21] K. Kuroki, and R. Arita, *J. Phys. Soc. Jpn.* **76**, 083707 (2007).
- [22] W. Koshibae, K. Tsutsui, and S. Maekawa, *Phys. Rev. B* **62**, 6869 (2000).
- [23] G. S. Nolas, J. Sharp, and H. J. Goldsmid, *Thermoelectrics : Basic Principles and New Materials Developmemts* Springer, Berlin (2001).
- [24] K. Behnia, D. Jaccard, and J. Flouquet, *J. Phys.: Condens. Matter* **16**, 5187 (2004).
- [25] P. Sun, N. Oeschler, S. Johnsen, B. B. Iversen, and F. Steglich, *Appl. Phys. Express* **2**, 091102 (2009).
- [26] P. Sun, N. Oeschler, S. Johnsen, B. B. Iversen, and F. Steglich, *Phys. Rev. B* **79**, 153308 (2009).
- [27] C. Petrovic, Y. Lee, T. Vogt, N. Dj. Lazarov, S. L. Bud'ko, and P. C. Canfield, *Phys. Rev. B* **72**, 045103 (2005).
- [28] J. B. Goodenough, *J. Solid State Chem.* **5**, 144 (1972).
- [29] C. Petrovic, J. W. Kim, S. L. Bud 'ko, A. I. Goldman, P. C. Canfield, W. Choe, and G. J. Miller, *Phys. Rev. B* **67**, 155205 (2003).
- [30] G. Appli and Z. Fisk, *Comments Condens. Mater. Phys.* **16**, 155 (1992).
- [31] B. C. Sales, E. C. Jones, B. C. Chakoumakos, J. A. Fernandez-Baca, H. E. Harmon, J. W. Sharp, and E. H. Volckmann *Phys. Rev. B* **50**, 8207 (1994).
- [32] T. Jarlborg, *Phys. Rev. B* **59**, 15002 (1999).
- [33] D. Mandrus, J. L. Sarrao, A. Migliori, J. D. Thompson, and Z. Fisk, *Phys. Rev. B* **51**, 4763 (1995).

- [34] P. Sun, N. Oeschler, S. Johnsen, B. B. Iversen, and F. Steglich, *J. Phys.: Conference on Low Temperature Physics* **150**, 012049 (2009).
- [35] J. M. Tomczak, K. Haule, T. Miyake, A. Georges, and G. Kotliar, *Phys. Rev. B* **82**, 085104 (2010).
- [36] T. Shibauchi, N. Katase, T. Tamegai, K. Uchinokura, T. Takabatake, G. Nakamoto, and A. A. Menovsky, *Phys. Rev. B* **56**, 8277 (1997).
- [37] T. Takabatake, Y. Echizen, T. Yoshino, K. Kobayashi, G. Nakamoto, H. Fujii, and M. Sera, *Phys. Rev. B* **59**, 13878 (1999).
- [38] P. P. Debye and E. M. Conwell: *Phys. Rev.* **93** (1954) 693.
- [39] H. P. R. Frederikse and E. V. Mielczarek, *Phys. Rev.* **99**, 1889 (1955).
- [40] H. P. R. Frederikse, *Phys. Rev.* **92**, 248 (1953).
- [41] L. Weber and E. Gmelin, *Appl. Phys. A* **53**, 136 (1991).
- [42] P. J. Moria and J. P. Maita, *Phys. Rev.* **96**, 28 (1954).
- [43] P. P. Debye and E. M. Conwell, *Phys. Rev.* **93**, 693 (1954).
- [44] M. Sasaki, G. X. Tai, S. Tamura, and M. Inoue, *Phys. Rev. B* **47**, 6216 (1993).
- [45] J. S. Kim, *J. Appl. Phys.* **86**, 3187 (1999).
- [46] R. Hu, V. F. Mitrović, and C. Petrovic, *Appl. Phys. Lett.* **92**, 182108 (2008).
- [47] J. F. Woods and C. Y. Chen, *Phys. Rev.* **135**, A1462 (1964).
- [48] A. Kawabata, *J. Phys. Soc. Jpn.* **49**, 628 (1980).
- [49] C. Herring, *Phys. Rev.* **96**, 1163 (1954).
- [50] P. Sun, M. Sondergaard, Y. Sun, S. Johnsen, B. B. Iversen, and F. Steglich, *Appl. Phys. Lett.* **98**, 072105 (2011).
- [51] J. C. Cooley, M. C. Aronson, and P. C. Canfield, *Phys. Rev. B* **55**, 7533 (1997).
- [52] T. Hiraoka, E. Kinoshita, H. Tanaka, T. Takabatake, and H. Fujii, *J. Magn. Magn. Mater.* **153**, **124** (1996).

- [53] J. Beille, M. B. Maple, J. Wittig, Z. Fisk and L. E. DeLong, *Phys. Rev. B* **28**, 7397 (1983).
- [54] F. Iga, M. Kasaya, H. Suzuki, Y. Okayama, H. Takahashi, and N. Mori, *Physica B* **186-188**, 419 (1993).
- [55] R. I. Boughton, J. L. Olsen, and C. Palmy, *Progress in Low Temp. Physics vol.VI* (edited by C. J. Gorter) North-Holland, Amsterdam (1970).
- [56] X. Wu, G. S. Neumann, S. Qin, M. Kanzaki, and L. Dubrovinsky, *J. Phys.: Condens. Matter* **21**, 185403 (2009).
- [57] N. W. Ashcroft, and N. D. Mermin, *Solid state Physics* Saunders College Publishing, (1988).
- [58] W. Paul, *J. Appl. Phys.* **32**, 2082 (1961).
- [59] A. Mani, J. Janaki, A. T. Satya, T. G. Kumary, and A. Bharathi, *J. Phys.: Condens. Matter* **24**, 075601 (2012).
- [60] J. D. Thompson, *Physica B* **223-224**, 643 (1996).
- [61] S. H. Liu, *Handbook on Physics and Chemistry of Rare Earths vol.17* Elsevier, North-Holland (1993).
- [62] A. Herzog, M. Marutzky, J. Sichelschmidt, F. Steglich, S. Kimura, S. Johnsen, and B. B. Iversen, *Phys. Rev. B* **82**, 245205 (2010).

Published work

- [1] H. Takahashi, R. Okazaki, I. Terasaki and Y. Yasui;
“Origin of the energy gap in the narrow-gap semiconductor FeSb₂ revealed by high-pressure magnetotransport measurements”
Phys. Rev. B, **88**, 165205 (2013).
- [2] H. Takahashi, N. Raghavendra, F. Gascoin, D. Pelloquin, S. Hebert and E. Guilmeau.; “Transport properties of an intermetallic with pseudo-hollandite structure as potential thermoelectric materials: the example of Tl_xCr₅Se₈”
Chem. Mater. **25**, 1809 (2013)
- [3] H. Takahashi, R. Okazaki, Y. Yasui and I. Terasaki;
“Low-temperature magnetotransport of the narrow-gap semiconductor FeSb₂”
Phys. Rev. B, **84**, 205215 (2011).
- [4] H. Takahashi, Y. Yasui, I. Terasaki and M. Sato.;
“Effects of ppm-level imperfection on the transport properties of FeSb₂ single crystals.”
J. Phys. Soc. Jpn. **80**, 054708 (2011).
- [5] M. Sato, Y. Kobayashi, S C. Lee, H. Takahashi, E. Satomi, and Y. Miura.;
“Studies on Effects of Impurity Doping and NMR Measurements of La1111 and/or Nd1111 Fe-Pnictide Superconductors”
J. Phys. Soc. Jpn. **79**, 014710 (2010).
- [6] Y. Kobayashi, S. C. Lee, H. Takahashi, T. Moyoshi, and M. Sato.;
“NMR studies on the superconducting symmetry of iron pnictide systems.”
Physica C. **470**, S472 (2010).
- [7] M. Sato, Y. Kobayashi, S. C. Lee, H. Takahashi and T. Moyoshi.;
“Distinct physical behaviors of LaFe_{1-y}Co_yAsO_{0.89}F_{0.11} between the superconducting and nonsuperconducting metallic regions of y divided by y ~ 0.05.”
Physica C. **470** S475 (2010).

International conference

- [1] H. Takahashi, R. Okazaki, Y. Yasui, I. Terasaki,
“High-mobility magnetotransport of narrow-gap semiconductor FeSb₂”
International Conference on Magnetism, AF0663, Korea, (July 2012).
- [2] H. Takahashi, S. Hebert, D. Pelloquin, F. Gascoin, R. Nunna, A. Maig-
nan, I. Terasaki
“Magnetic and transport properties of Hollandite systems”
European Materials Research Society, France, (May 2012).
- [3] H. Takahashi, R. Okazaki, Y. Yasui, I. Terasaki, M. Sato,
“High-mobility transport of FeSb₂ with ppm-level carrier concentration: A
relationship to the huge thermopower, International conference on thermo-
electric”
International conference on thermoelectric, USA, (July 2011).

Acknowledgements

This doctoral research would not be completed without supports of many people. I would like to express my appreciation to all of them. First of all, I would like to thank Professor Ichiro Terasaki for his great advice and support during this research. I learned not only how to develop the research, but also to enjoy this work from his scientific attitude. I would like to express my gratitude to Professor Masatoshi Sato for the initial motivation and valuable advice and discussion in this study. I would like to acknowledge Professor Yukio Yasui for his helpful advice and discussion. I wish to express my appreciation to Dr. Ryuji Okazaki. He provided extensive advice with the experimental methods and analysis. I am extremely grateful to Dr. Sylvie Hebert for her kind help for study and life in France, which become variable experience for me. I also thank all staffs and students in CRISMAT institute in France. I would like to thank Professor Hiroki Taniguchi for the technical advice of experiments. I wish to appreciate Professor Hiroshi Kontani, and Professor Akito Kobayashi for their helpful discussion. I would like to thank the staffs of Low Temperature Laboratory for providing liquid helium and nitrogen. I also thank members in Laboratory of Condensed-Matter Physics of Functional Materials. I wish to acknowledge the financial support provided by the Research Fellowship of the Japan Society for Promotion of Science for Young Scientists, Nagoya University Program for Leading Graduate Schools, and FP7 European Initial Training Network SOPRANO. Finally, I am deeply indebted to my parents and my family, who always supported and encouraged me in many ways.